Explicit habit-prediction in the Lagrangian super-particle ice microphysics model McSnow

Jan-Niklas Welss[1,2], **C. Siewert**[1], **A. Seifert**[1]

[1]Deutscher Wetterdienst, Frankfurt, Germany
[2]Institute for Atmospheric Physics, Johannes Gutenberg University Mainz, Mainz, Germany

Key Points:

- McSnow is extended by an explicit habit prediction including the revision of corresponding parameterizations.
- A new inherent growth ratio overcoming existing deficiencies is proposed.
- The impact of the modifications on the depositional growth, aggregation, and riming is shown for two distinct case studies.

Corresponding author: Jan-Niklas Welss, jwelss@uni-mainz.de

Abstract

The Monte-Carlo ice microphysics model McSnow is extended by an explicit habit prediction scheme, combined with the hydrodynamic theory of Böhm. Böhm's original cylindrical shape assumption for prolates is compared against recent lab results, showing that interpolation between cylinder and prolate yields the best agreement. For constant temperature and supersaturation, the predicted mass, size, and density agree well with the laboratory results, and a comparison with real clouds using the polarizability ratio shows regimes capable of improvement. An updated form of the inherent growth function to describe the primary habit growth tendencies is proposed and combined with a habit-dependent ventilation coefficient. The modifications contrast the results from general mass size relations and significantly impact the main ice microphysical processes. Depending on the thermodynamic regime, ice habits significantly alter depositional growth and affect aggregation and riming.

Plain Language Summary

The McSnow model was extended to predict the shape of ice crystals. A comparison of the falling behavior of modeled and 3D-printed ice crystals shows a discrepancy that can be improved by interpolation. At constant temperature and supersaturation, simulated crystal properties agree well with laboratory results, and by comparison to real clouds, we have updated the function to describe growth tendencies. Ice shape is shown to have a significant influence on the main microphysical processes.

1 Introduction

Inside clouds, atmospheric conditions are highly variable, often containing gaseous, liquid, and frozen water simultaneously in spatial and temporal heterogeneity (e.g. Morrison et al., 2012). The complex transitions involving all three phases are challenging when trying to describe and understand the microphysical processes within mixed-phase clouds (Morrison et al., 2020). Interactions involving ice crystals are tricky because of the variety of possible shapes. These habit characteristics are critical for the cold phase microphysical processes that influence sedimentation, deposition/sublimation, riming, aggregation, and especially radiative properties. Specialized observational methods to gather information on the rates of ice-microphysical processes are constantly being developed and improved, ranging from ground and in-situ (e.g. Field et al., 2004; Locatelli & Hobbs, 1974) to remote sensing observations (e.g. Dias Neto et al., 2019; Tridon et al., 2019). Classification and categorization of observed ice particles is an ongoing task (Bailey & Hallett, 2009; Kikuchi et al., 2013). This helps to link the occurrence of ice crystal types to specific atmospheric conditions. While these efforts provide data sets covering a variety of variables, they only partially allow attribution of effects to individual processes. Laboratory measurements such as Takahashi et al. (1991) or Connolly et al. (2012) allow process isolation, but lack representation of the full range of atmospheric conditions and especially the transition from isolation to a fully interactive system. As a result, the resulting physical descriptions can become highly specialized and are often only generalizable by assuming certain atmospheric conditions or categorizing ice habit, introducing artificial thresholds. The challenge posed by individual growth histories under changing conditions is to describe the variety of simple (columns, plates) and more complex (branched and polycrystalline) ice habits coexisting with aggregates composed of crystals of different shapes and numbers. Mass-size and mass-area relations may be able to describe the average geometry of certain ice habits (Mitchell, 1996; Auer & Veal, 1970; Um et al., 2015), but cannot represent the natural variety and transitions due to the use of thresholds. Overcoming the threshold between ice categories to allow a natural transition is a goal of modern microphysical schemes (Morrison & Grabowski, 2008; Milbrandt et al., 2021). Previous studies show that it is generally beneficial to explicitly resolve habit

development to improve the microphysical representation of ice in models: Jensen et al. (2017) show an effect of ice habit on the spatial precipitation pattern, Hashino and Tripoli (2007) find that dendrites extend dendritic growth regions further than atmospheric conditions suggest, and Sulia and Harrington (2011) conclude that the absence of ice habit underestimates ice growth and cloud glaciation time. Also, only models that resolve the evolving crystal shapes can make use of the wealth of data provided by radar polarimetry (Trömel et al., 2021) and combine the approaches to identify gaps in the interpretation of observations as well as in the microphysical descriptions when modeling clouds and precipitation (von Terzi et al., 2022).

To fully evaluate the effects of dynamically developing habits, detailed descriptions of processes at the particle level are needed. The approach of J.-P. Chen and Lamb (1994b) simplifies the ice habits of individual crystals as porous spheroids. The scheme predicts the shape and density of ice particles, helping to depict the natural evolution of ice habits and minimizing artificial type classification. While no natural crystal resembles a spheroid, Jayaweera and Cottis (1969) show that spheroids are suitable for representing columnar or plate-like ice crystals. However, even a simplified geometry requires changes in the process description: Vapor growth depends crucially on the particle shape, which affects the water vapor field around the particle. The theoretical framework of Böhm allows the consideration of ice habits for fall speed and collision effects based on spheroids (Böhm, 1989, 1992a, 1992b, 1992c, 1994, 1999). Based on investigations for oblates (Pitter et al., 1974), Hall and Pruppacher (1976) deduce that the ventilation is independent or only slightly dependent on the particle shape, but recent results suggest that this assumption underestimates the ventilation for prolate particles of larger sizes (Wang and Ji (2000), Ke et al. (2018) and others). For the collision of ice crystals with droplets, the results of Wang and Ji (2000) suggest the existence of preferred riming regions depending on the Reynolds number, which are difficult to represent in the spheroidal approach. Jensen and Harrington (2015) propose a way to distribute rime on the particle surface perpendicular to the flow in an effort to evaluate the effect of ice habits on the onset of riming.

The likelihood of ice crystal aggregation is enhanced by non-spherical geometry models because an increased cross-sectional area is a direct factor. However, it is difficult to describe the geometry of the resulting aggregates because of the many degrees of freedom involved in the collision event. Several descriptions attempt to characterize the geometry of aggregates after collisions (J.-P. Chen & Lamb, 1994a; Shima et al., 2020; Gavze & Khain, 2022) but a general and accurate parameterization is not yet available.

This paper presents the results of the extension of the Monte Carlo ice microphysics model *McSnow* Brdar and Seifert (2018) by an explicit habit prediction (HP) scheme using porous spheroids following J.-P. Chen and Lamb (1994b, CL94) and Jensen and Harrington (2015, JH15) to replace the classical m-D relations. The model uses the complete theoretical framework of Böhm, allowing the consideration of ice habits for fall velocity and collision effects (Sec. 2.2). We show that the original shape assumption for prolates underestimates the fall velocity derived from recent laboratory studies, and provide an interpolation to overcome the observed mismatch (Sec. 3.1). The original formulation of the ventilation effect (Hall & Pruppacher, 1976) is extended to include a habit-specific ventilation effect suggested by several studies. We evaluate the performance of the habit prediction scheme against laboratory results and polarimetric observations, and propose several changes to overcome identified deficiencies. These include changes to the Inherent Growth Function (IGF) and the plate branching criterion. For the full model, we present the effects of explicit habit formation on deposition, riming, and aggregation in a 1-D snow shaft setup (Sec. 5).

2 Habit dependence of microphysical processes

This section describes the extensions of *McSnow* (Brdar & Seifert, 2018) regarding the habit prediction scheme, including necessary changes and clarifications encompassed by an explicit ice morphology.

2.1 Habit prediction

In nature, the geometry and internal structure of ice particles can reach a high degree of complexity that defies any explicit description. A common approach is the use of z axis symmetric spheroids based on the two defining semi-axes a (equatorial) and c (polar radius). We can assume that the approximation of oblate and prolate spheroids for the two dominant primary habits of plates and columns is superior to fixed mass-size (m-D), mass-area (m-A), and size-density (D-ρ) relations because this removes the need for categorization of crystal and allows the transition between ice shapes to be considered. The aspect ratio ϕ (ratio of polar to equatorial radius) describes the shape of the spheroid

$$\phi = \frac{c}{a}, \tag{1}$$

$$V_\mathrm{i} = \frac{4}{3}\pi a^3 \phi = \frac{4}{3}\pi a^2 c, \tag{2}$$

$$\rho_\mathrm{app} = \frac{m_\mathrm{i}}{V_\mathrm{i}}. \tag{3}$$

To account for possible secondary habit effects such as branching and hollowing, we use the ice volume V_i and the apparent density ρ_app. With the introduction of explicit particle geometry, the shape changing processes must be adjusted, including vapor deposition, riming, and aggregation. Based on the results of J. Nelson (1998) and Harrington et al. (2019), we assume that the aspect ratio remains unchanged during sublimation. Mitra et al. (1990) and Kintea et al. (2015) find a similar behavior for melting, but the question remains whether water fills gaps revealed by branched or rimed structures, possibly changing the density of the particles but not necessarily their shape.

2.1.1 Deposition/Sublimation

The equation for mass change through vapor deposition and sublimation,

$$\left(\frac{\mathrm{d}m_\mathrm{i}}{\mathrm{d}t}\right)_\mathrm{v} = 4\,\pi\,C\,D_\mathrm{v}\,f_\mathrm{v}\,\frac{p_\mathrm{vap} - p_\mathrm{sat,i}}{R_\mathrm{v}\,T}\,\left(1 + \frac{L_\mathrm{s}^2\,D_\mathrm{v}\,p_\mathrm{sat,i}}{K_\mathrm{d}\,R_\mathrm{v}^2\,T^3}\right)^{-1}, \tag{4}$$

considers the shape information mainly via the capacitance C. The other variables are the vapor diffusivity D_v, the ventilation coefficient f_v, the vapor pressure p_vap, the saturation pressure with respect to ice $p_\mathrm{sat,i}$, as well as the temperature T, the gas constant of water vapor R_v, the latent heat of sublimation L_s, and the thermal conductivity of dry air K_d. While J. T. Nelson and Baker (1996) show that the classical capacitance model cannot evolve faceted crystals because of inconsistent surface boundary conditions, it still produces relatively accurate estimates for mass and shape evolution. Still, Westbrook et al. (2008) show that the actual capacitance might depend on the internal structure of the hydrometeor, eventually causing an overestimation of capacitance for hydrometeors of reduced density when using the original formulation of CL94.

Kobayashi (1961) shows that the evolution of primary habits (planar or columnar) depends mainly on ambient temperature, while that of secondary habits (branching and hollowing) depends on supersaturation. To quantify the temperature regimes favoring certain geometries, CL94 derive an inherent growth function Γ (IGF) by collecting laboratory and in-situ measurements for the temperature range between 0 ° and -30 °C (respectively $243 - 273\,\mathrm{K}$) by relating individual growth along the two major axes

$$\Gamma(T) = \frac{\mathrm{d}\ln c}{\mathrm{d}\ln a}\,. \tag{5}$$

The change in crystal mass causes an ice volume change

$$\mathrm{d}V_\mathrm{i} = \frac{1}{\rho_\mathrm{depo.}}\,\mathrm{d}m_\mathrm{i}\ , \tag{6}$$

with the deposition density $\rho_\mathrm{depo.}$. The spheroid shape does not explicitly allow for secondary habits. To capture branching and hollowing, the volume of the circumscribing spheroid is modified. Physically, the air inside the spheroid lowers the apparent density below ice density. J.-P. Chen and Lamb (1994b) use an empirical formulation for the deposition density based on experimental results of Fukuta (1969). We prefer the direct parameterization of the deposition density using the IGF proposed by Jensen and Harrington (2015, JH15)

$$\rho_\mathrm{depo} = \begin{cases} \rho_\mathrm{i}\,\Gamma(T) & , \quad \Gamma < 1\ , \\ \rho_\mathrm{i}\,\Gamma^{-1}(T) & , \quad \Gamma \geq 1\ . \end{cases} \tag{7}$$

For oblates ($\phi < 1$), branching happens only if $v\,a > \pi\,D_\mathrm{v}\,c$ (JH15), otherwise $\rho_\mathrm{depo} = \rho_\mathrm{i}$. For prolates, hollowing happens immediately.

Using the same deposition density of branching/hollowing for sublimation may lead to unphysical apparent densities because the IGF is only valid for temperature and supersaturation during the deposition process. Laboratory measurements suggest that ice particles preserve their shape during sublimation, maintaining a constant aspect ratio (Harrington et al., 2019; J. Nelson, 1998). We use the apparent density for particles undergoing sublimation ($\rho_\mathrm{depo} = \rho_\mathrm{app}$).

Following CL94, we can predict the change in aspect ratio using the IGF

$$\mathrm{d}\ln\phi = \frac{\Gamma - 1}{\Gamma + 2}\,\mathrm{d}\ln V_\mathrm{i}\ . \tag{8}$$

The evolution of V_i follows from Eqs. (4) and (6). As in previous work (Korolev & Isaac, 2003; Lawson et al., 2008; Baran, 2012), we restrict habit development for now to occur only for particles larger than $D \geq 10\,\mu m$, since observations suggest that crystals up to this size are approximately spherical.

The ice habit also affects the airflow around the particle and ventilation. The parts of the crystal surface that extend farthest into the flow experience the greatest effect due to increased water vapor advection (J.-P. Chen & Lamb, 1994b). Hall and Pruppacher (1976) suggest a description of the ventilation coefficient by

$$f_\mathrm{v} = b_1 + b_2\,X_\mathrm{v,equiv}^{\gamma}\ , \tag{9}$$

the constants b_1, b_2, and γ have been generalized from observations for spheres and plates as

$$\begin{aligned} b_1 &= 1.0, & b_2 &= 0.14, & \gamma &= 2 & &\text{for } X_\mathrm{v,equiv} \leq 1\ , \\ b_1 &= 0.86, & b_2 &= 0.28, & \gamma &= 1 & &\text{for } X_\mathrm{v,equiv} > 1\ . \end{aligned}$$

The proposed ventilation is a function of Schmidt N_Sc and Reynolds number $N_\mathrm{Re,equiv}$

$$X_\mathrm{v,equiv} = N_\mathrm{Sc}^{\frac{1}{3}}\,N_\mathrm{Re}^{\frac{1}{2}}\ , \tag{10}$$

$$N_\mathrm{Sc} = \frac{\mu_\mathrm{a}}{\rho_\mathrm{a}\,D_\mathrm{v}}\ , \tag{11}$$

$$N_\mathrm{Re,equiv} = \frac{d_\mathrm{equiv}\,v_\mathrm{t}\,\rho_\mathrm{a}}{\mu_\mathrm{a}}\ . \tag{12}$$

The dynamic viscosity μ_a can be described by Sutherland's Law (Sutherland, 1893)

$$\mu_\mathrm{a}(T) = \mu_0\,\frac{T_0 + T_\mathrm{S}}{T + T_\mathrm{S}}\left(\frac{T}{T_0}\right)^{3/2}\ , \tag{13}$$

with $\mu_0 = 1.716 \times 10^{-5}$, the melting/freezing point $T_0 = 273.15\,\mathrm{K}$, and the Sutherland temperature $T_\mathrm{S} = 110.4\,\mathrm{K}$. The other variables are the air density ρ_a, the volume-equivalent diameter of a sphere d_equiv, and the terminal velocity v_t. Pruppacher and Klett (1997) collected habit-specific solutions for selected N_Re-regimes, but no continuous description for all habits is known to the authors. We propose a habit-dependent formulation based on several numerical studies in Section 4.1.

Ventilation affects the geometric evolution by favoring the edges of the crystals. To account for this effect, we replace the IGF of Eq. 8 by the ventilation-influenced growth habit Γ^* as proposed by CL94

$$\Gamma^* = \Gamma\, f^* \ , \tag{14}$$

where the ratio of the local ventilation coefficients f^* of the respective axis (f_c, f_a)

$$f^* = \frac{f_c}{f_a} \approx \frac{b_1 + b_2\, X^\gamma\, (\frac{c}{r_0})^{1/2}}{b_1 + b_2\, X^\gamma\, (\frac{a}{r_0})^{1/2}} \ , \tag{15}$$

is used instead of the overall ventilation coefficient f_v. The local ventilation coefficient compares the local axis dimension to the radius of a sphere r_0 with the same volume.

The maximum dimension is defined as $D = 2\max(a, c)$. We distinguish between the projected area A, which is relevant for riming and collision processes, and the hydrodynamic area $\tilde{A}$. The geometric area A of a spheroid is defined as the circumscribing ellipse

$$\begin{aligned} A_\mathrm{prolate} &= \pi\, a\, c \qquad && \text{for prolates,} \\ A_\mathrm{oblate} &= \pi\, a^2 \qquad && \text{for oblates,} \end{aligned} \tag{16}$$

while the cross-sectional area $\tilde{A}$ is the effective area presented to the flow (cf. Böhm (1989)). JH15 suggest a linear dependency on ϕ and ρ_app to link the degree of branching to the thickness of a plate

$$\begin{aligned} \tilde{A} &= \xi\, A \\ \xi &= (1-\phi)\left(\frac{\rho_\mathrm{app}}{\rho_\mathrm{i}}\right) + \phi \qquad && \text{for oblates,} \\ \xi &= 1 \qquad && \text{for prolates.} \end{aligned} \tag{17}$$

A decrease in cross-sectional area represents flow through the porous structures of the particle, which in turn reduces flow resistance. Prolates are assumed to be hollow inwards, so the cross-sectional area is effectively unaffected ($A = \tilde{A}$). In terms of collision probability, we will see that the theory of Böhm uses boundary layer theory, explicitly considering the difference between geometric and cross-sectional area via the area ratio q (cf. Eq. 23), which is similar to ξ above.

2.1.2 Riming

The distribution of rime along the two major axes is a critical factor in the prediction of ice crystal habit. We assume that particles fall with their largest cross-sectional area perpendicular to the flow, so that rime is always added to the minor axis while preserving the maximum dimension, transforming the habit of the particle towards a quasi-spherical shape. Jensen and Harrington (2015) refer to the work of A. J. Heymsfield (1978) for observations of the aspect ratio of graupel and propose that this quasi-spherical shape translates into an aspect ratio of $\phi = 0.8$ for plates or equivalently $\phi = 1/0.8 = 1.25$ for columns. For prolates with an aspect ratio between $1 < \phi \leq 1.25$, the updated equatorial radius a can be described as

$$a = \sqrt{\frac{V_\mathrm{tot} + \frac{\Delta m_\mathrm{rime}}{\rho_\mathrm{rime}}}{\frac{4\pi}{3} c}} \ , \tag{18}$$

with V_{tot} the total volume before riming. Analogous, for oblate particles with $0.8 < \phi \leq 1$

$$c = \frac{V_{\text{tot}} + \frac{\Delta m_{\text{rime}}}{\rho_{\text{rime}}}}{\frac{4\pi}{3} a^2} \ . \tag{19}$$

The choice of a quasi-spherical aspect ratio threshold can lead to an oscillation around these values if simultaneous depositional growth supports the development of a more pronounced habit. These oscillations can be interpreted as a tumbling of the graupel particle, so that the newly added mass is randomly added to one of the axes.

We combine habit prediction with the stochastic riming approach of *McSnow*, introduced by Seifert et al. (2019), since it incorporates the shape properties of the particle into the collision probability using the theory of Böhm via the Stokes number (cf. Sec. 2.2.2). To better understand the feedback between habit information and collision probability, we will take a closer look at the implications of the shape dependence of the collision kernel.

2.1.3 Aggregation

For aggregates, we rely on the diagnostic geometry introduced by Brdar and Seifert (2018) following the empirical power laws for the mass-size-relation of aggregates (Mitchell, 1996, S3: Aggregates of Side Planes, Columns, and Bullets). The formulation and implementation of a more advanced aggregation framework that takes into account the habits and properties of the colliding particles in a self-consistent manner is left for future work (J.-P. Chen & Lamb, 1994a; Shima et al., 2020; Gavze & Khain, 2022). For small numbers of monomers ($N_{\text{m}} < 10$), we expect that this rather simple empirical approach may lead to errors in the estimation of particle properties (Karrer et al., 2021) compared to the explicit ideas above. The approach does not describe the transition from aggregates defined by the shape of a few individual monomer habits to those consisting of many particles.

To describe the aggregation of hydrometeors, we use the Monte-Carlo algorithm of Shima et al. (2009). When using an explicit habit prediction, aggregates and the assumption about the geometry term of the collision kernel K must be taken into account. In classical m-D- and m-A-relations, the maximum dimension D is used to estimate the geometry term (D-Kernel)

$$K_D = \pi \left(\frac{D_1}{2} + \frac{D_1}{2} \right)^2 S \, E_{\text{c}} \, |v_1 - v_2| = \pi \, (r_1 + r_2)^2 \, S \, E_{\text{c}} \, |v_1 - v_2| \ , \tag{20}$$

where S is the sticking efficiency, E_{c} is the collision efficiency (see Sec.2.2.2), and v_n is the terminal fall velocity of the individual particles. The formulation is neutral for the treatment of oblates, but may overestimate the actual collision cross section of a prolate. An alternative is the A-Kernel (Böhm, 1994; Connolly et al., 2012; Karrer et al., 2021), which uses the equivalent radius $r_{n,\text{eq}} = \sqrt{A_n \, \pi^{-1}}$

$$K_A = \pi \left(\sqrt{A_1 \, \pi^{-1}} + \sqrt{A_2 \, \pi^{-1}} \right)^2 S \, E_{\text{c}} \, |v_1 - v_2| = \pi \, (r_{1,\text{eq}} + r_{2,\text{eq}})^2 \, S \, E_{\text{c}} \, |v_1 - v_2| \ . \tag{21}$$

The overestimation can be determined by the ratio of the maximum dimension of the prolates D_{max} to the equivalent diameter $D_{n,\text{eq}}$ and is proportional to

$$\frac{D_{\text{max}}}{D_{n,\text{eq}}} = \frac{2\,c}{2\,\sqrt{A_n \, \pi^{-1}}} = \frac{c}{\sqrt{a\,c}} = \sqrt{\frac{c}{a}} = \sqrt{\phi} \ . \tag{22}$$

We favor the use of the A-kernel when using the habit prediction scheme.

2.2 Review of Boehm's terminal velocity and collision efficiency parameterization

The work of Böhm comprises several publications, making it difficult to extract the parameterizations for terminal velocity and collision efficiency from his original work (Böhm,

1989, 1992a, 1992b, 1992c, 1994, 1999). Therefore, we review and summarize his work and its application to habit prediction. Since Böhm (2004) advised to use the original equations because they compare better with numerical simulations and field observations, we exclude the revision of Posselt et al. (2004).

2.2.1 Terminal velocity

The terminal velocity scheme is important for particles with different shapes and directly affects the depositional growth and the collision kernel. Böhm's parameterization is a generalized and complete framework that makes the following necessary assumptions

- The maximum dimension is oriented in the horizontal plane, as shown for example by Westbrook and Sephton (2017) for all simple geometries studied.
- The porosity p in the theory of Böhm is related to the ratio of the cross-sectional area $\tilde{A}$ to the circumscribing ellipsis area A_{ce}. It represents the internal structure of ice crystals caused by secondary habits

$$p = 1 - q, \qquad q = \frac{\tilde{A}}{A_{\mathrm{ce}}} \ . \tag{23}$$

  The ratio q is not to be confused with the area ratio $A_{\mathrm{r}} = \tilde{A}\, A_{\mathrm{cc}}^{-1}$ which A. J. Heymsfield and Westbrook (2010) and McCorquodale and Westbrook (2021) define as the ratio of the cross-sectional area to the circumscribing circle A_{cc}.
- Böhm (1992a) argues that the hydrodynamic behavior of prolate particles is similar to that of cylinders. He suggests

$$q = \frac{4}{\pi} \qquad \text{for } \phi > 1 \ .$$

  This approximation is discussed in detail in Section 3.1.
- We add the assumption that all particles accelerate immediately to their terminal velocity. See, e.g., Naumann and Seifert (2015) for an alternative approach that attempts to account for deviations from the terminal fall velocity.

Böhm's parameterization is valid for solid and liquid hydrometeors and is based on a functional dependence of the drag coefficient on the Reynolds number derived from Boundary Layer Theory (BLT). The terminal velocity follows the definition of the Reynolds number. Both the Reynolds number and the drag coefficient are modified by the aspect ratio via the Best number (see Eq. A1).

Böhm (1992a) showed that the formula is consistent with viscous theory, and by matching the results from BLT with Oseen's theory (Oseen, 1927), there is good agreement of inertial drag at low Reynolds numbers. Böhm (1992a) claims that the errors are generally on the order of $\epsilon \leq 10\,\%$ for $0 < N_{\mathrm{Re}} < 5 \times 10^5$ for the hydrometeor types studied (raindrops, columnar and planar ice crystals, rimed and unrimed aggregates, various types of graupel, and hail). The complete parameterization of the fall velocity can be found in the appendix A1.

2.2.2 Collision efficiency

Generally, the collision efficiency E_{c} is defined as the ratio of the actual collision cross section to the geometric one (Pruppacher & Klett, 1997)

$$E_{\mathrm{c}} = \frac{x_c^2}{(r_1 + r_2)^2} = \frac{y_s}{\delta} \ , \tag{24}$$

where x_c is the initial horizontal offset and r_n is the radius of the interacting particles. Böhm (1992b) states that the collision efficiency for axisymmetric particles can be described by the ratio of the stop distance of the collected particle y_s and the boundary

layer thickness of the collecting particle δ. For non-axisymmetric particles, the collision efficiency derivation is extended to a generalized form (Böhm, 1992c)

$$E_{\mathrm{c}} = \left(\frac{y_s}{\delta}\right)^{2/j} \ , \tag{25}$$

with $j = 1$ for a two-dimensional flow (around the prolate) and $j = 2$ for the axisymmetric case. The boundary layer thickness δ can be calculated by

$$\delta = \delta_0 \, \frac{r}{\sqrt{N_{\mathrm{Re}} \, \Gamma_\phi}} \ , \tag{26}$$

with $\delta_0 = 3.60$ for oblates and $\delta_0 = 4.54$ for prolates The habit specific function Γ_ϕ can be found in the Appendix (Eq. A1c).

By replacing the individual boundary layer by the sum of the boundary layers of the colliding particles and integrating the differential equation from the initial velocity (detailed analysis in the dissertation (Böhm, 1990)), Böhm finds the collision efficiency for the resulting two-body system as

$$E_{\mathrm{c}} = \begin{cases} \left[H \, \ln\left(\cosh\frac{F}{H} + \frac{1+G}{F} \, \sinh\frac{F}{H}\right) - G\right]^{2/j}, & \left(\frac{F}{H} < 10\right) \ , \\ H \ln\left(\frac{F+G}{2F}\right) + F - G, & \left(\frac{F}{H} \geq 10\right) \ . \end{cases} \tag{27}$$

The details of the variables used can be found in A2.

To account for the contribution of the surrounding non-frictional flow, Böhm added an approximate analytical solution based on potential flow theory (cf. Böhm (1994)). This extension aims at improving the asymptotic behavior for low Reynolds numbers $N_{\mathrm{Re}} \lesssim 1$. With this modification, the total collision efficiency E is the product of the collision efficiency according to BLT E_{c} (from above) and the contribution from potential flow theory E_{p}

$$E = E_{\mathrm{c}} \, E_{\mathrm{p}} = \begin{cases} E_{\mathrm{c}} \left[\left(\cosh\frac{\Delta_x \, t_\delta}{c_x} + \frac{1}{\Delta_x} \sinh\frac{\Delta_x \, t_\delta}{c_x} \, e^{-t_\delta / c_x}\right)\right]^{-j}, & \left(b \, c_y \geq 1\right) \ , \\ E_{\mathrm{c}} \left[\left(\frac{2 \, \Delta_x}{1+\Delta_x} \, e^{-(\Delta_x - 1) \, t_\delta / c_x}\right)\right]^{j}, & \left(b \, c_y \leq 1\right) \ . \end{cases} \tag{28}$$

The full formulations of the variables used in Eq. 28 can also be found in Appendix A2. For the remainder of the paper, we will refer to the total collision efficiency E as E_{c}.

3 Discussion of Boehm's Theory for habit prediction

3.1 Shape assumptions for columns

For particles that change habit, the hydrodynamic assumption in Böhm's theory changes from a symmetric flow around an oblate to an asymmetric flow around a cylinder (cf. dashed lines in Fig. 3). This change in morphology between primary habits may not be fully transferable to natural ice geometries, where complex crystalline features such as capped columns may evolve instead of complete habit changes. It is unclear if and how the spheroidal approach could capture these effects. Recent laboratory results from McCorquodale and Westbrook (2021) provide data for over 80 particle geometries at different aspect ratios. McCorquodale and Westbrook (2021) also evaluate the performance of Böhm's original work (Böhm, 1989, B89) and criticize a general overestimation of the drag coefficient. We expect the modifications from (Böhm, 1992a) to (Böhm, 1999) including the dependency on the shape of the spheroidal to significantly improve the agreement with the lab data. The C_{d}-N_{Re} relationship of the latest formulation from Böhm is compared with the TRAIL results in Figure 1 and the data points for the *CO1* particle ($\phi = 1.0476$) from Westbrook and Sephton (2017). We re-scale the drag coefficient by the area ratio $A_{\mathrm{r}}^{1/2}$ compensates for the effect of A_{r} and allow comparison between the data and the derived C_{d}-N_{Re}-relation of A. J. Heymsfield and Westbrook

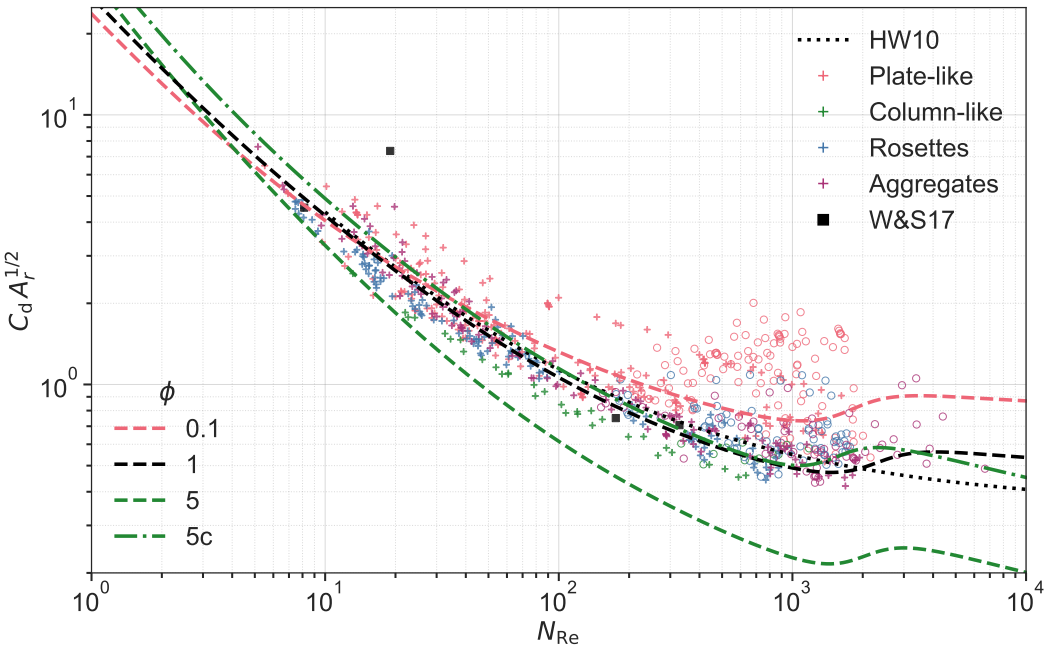

Figure 1. Comparison of measurements of N_{Re} and drag coefficient C_{d} for ice particle analogues (colored '+'/'∘' for steady/unsteady regimes) against the parameterization of Böhm. Black squares mark the data from Westbrook and Sephton (2017, W&S17) for a cylinder with $\phi = 1.0476$. The black dotted line marks the results from A. J. Heymsfield and Westbrook (2010), while the dashed colored lines show the results using the parameterization from Böhm for the corresponding ϕ.

(2010). The dashed and dash-dotted lines show three different ARs (color-coded) representing spherical ($\phi = 1$, black), plate-like ($\phi = 0.1$, red), and columnar/prolate particles ($\phi = 5$, green). Additionally, we include colored markers for the TRAIL results. The area ratio needs special attention when the scheme of Böhm is used for prolate particles, because the definition varies from that of q (Eq. 23). McCorquodale and Westbrook (2021) define the area ratio A_{r} as

$$A_{\mathrm{r}} = \tilde{A}\, A_{\mathrm{cc}} = q\, \phi^{-1} \ , \tag{29}$$

with $q = 1$ for prolate spheroids and $q = 4\,\pi^{-1}$ for cylinders. For all other hydrometeor types we assume $A_{\mathrm{r}} = 1$. The laboratory data and the parameterization agree well and the explicit dependence on the aspect ratio of the hydrometeors can capture the geometric effect of the different particle types. The drag coefficient of columnar particles differs significantly between the cylindrical and the prolate approach. At low Re, the prolate curve seems to reproduce the drag coefficient better. However, as Re increases, it greatly underestimates the drag and the cylindrical approach provides a better representation.

To better understand the difference in drag between cylindrical and spheroidal shapes, we compare the ϕ dependence of the parameterization with the laboratory results for prolate particles only. The combined data set consists of particles with $\phi = [1.0476, 2, 3, 5]$, allowing us to estimate the behavior near sphericity and the asymptotic behavior. Starting from low Reynolds numbers $N_{\mathrm{Re}} \approx 10^0$, the two geometries slowly diverge as can be seen in Figure 2. For $N_{\mathrm{Re}} > 10^2$, the prolate geometry agrees well with the two black squares marking the data of $\phi = 1.0476$, but has lower drag coefficients than the measurements for $\phi \geq 2$. The curves using the cylindrical assumption behave in the oppo-

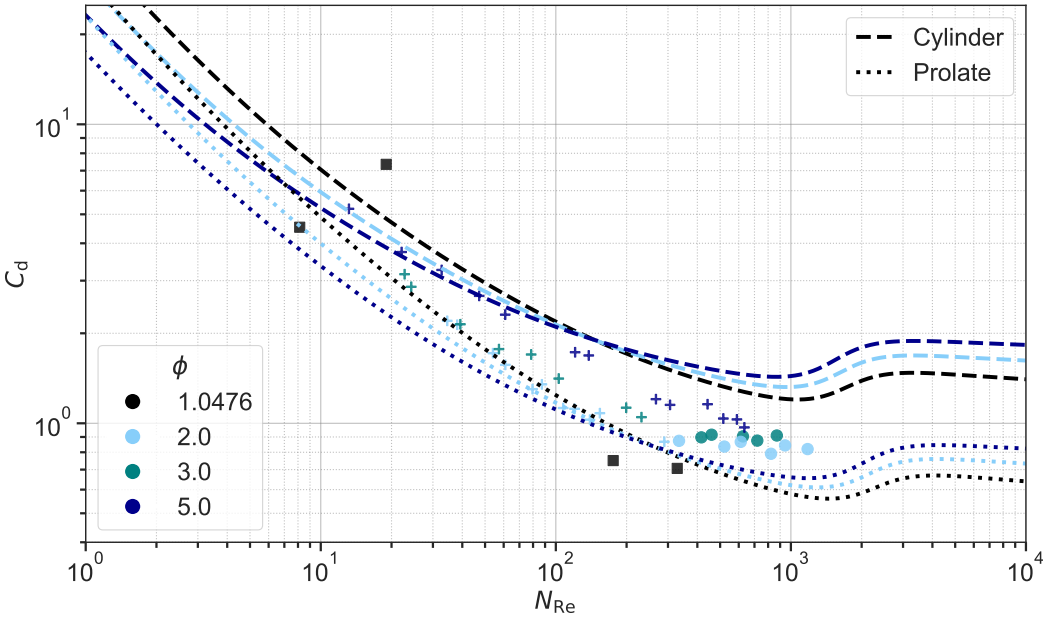

Figure 2. Comparison of N_{Re} and C_{d} for measured prolate ice particle analogues from McCorquodale and Westbrook (2021) ('+'/'∘' for steady/unsteady regimes) and Westbrook and Sephton (2017) (squares) against the parameterization of Böhm for different ϕ (color-coded) and assumed hydrodynamic assumption (short-dashed: prolate, long-dashed: cylinder).

site way and predict to high drag coefficients for $\phi \geq 2$ and especially overestimate the behavior for $\phi = 1.0476$. The majority of the measurements lie between the two assumptions. The disagreement for particles near sphericity explains the sudden deceleration of particles evolving from oblate or spherical particles into prolates when a cylinder is assumed and suggests a revision of this approach.

Using the original data from McCorquodale and Westbrook (2021), we derive a N_{Re}-C_{d} relation only for hexagonal columns (HCs) based on the area ratio A_{r} to describe the shape

$$C_{\mathrm{d}} = A_{\mathrm{r}}^{n} C_0 (1 + d_0 N_{\mathrm{Re}}^{-1/2})^2 \ . \tag{30}$$

The empirical values found are $n = -1/2$, $C_0 = 0.30$, and $d_0 = 7.1$, improving the agreement for HCs over the models of A. J. Heymsfield and Westbrook (2010) and McCorquodale and Westbrook (2021), which are generalized for all particle types (cf. Fig. A1). We use the empirical values obtained for Eq. (30) to extrapolate the behavior to other aspect ratios and corresponding terminal velocities. Particle characteristics are derived by similarity theory for specific data points of hexagonal columns. Figure 3 shows the fall speed as a function of aspect ratio $v_{\mathrm{t}}(\phi)$ for four particles of increasing mass. The black and dark blue line are representative for $\mathrm{Re} < 100$ and the light blue and grey line for particles with $100 < \mathrm{Re} < 1000$. Comparing the results from Böhm's scheme for the spheroidal (solid) and the cylindrical prolate assumption (dashed), shows the aforementioned deceleration near $\phi = 1$. The fall velocity behavior derived from the data of McCorquodale and Westbrook (2021) suggests a more subtle transition from a prolate to a cylindrical geometry and fits the results of Figure 2. The cylindrical geometry prescribes an edge at the basal surface, but physically the representation of this edge in the hydrodynamic properties is at least questionable in the spheroidal framework of habits. We therefore

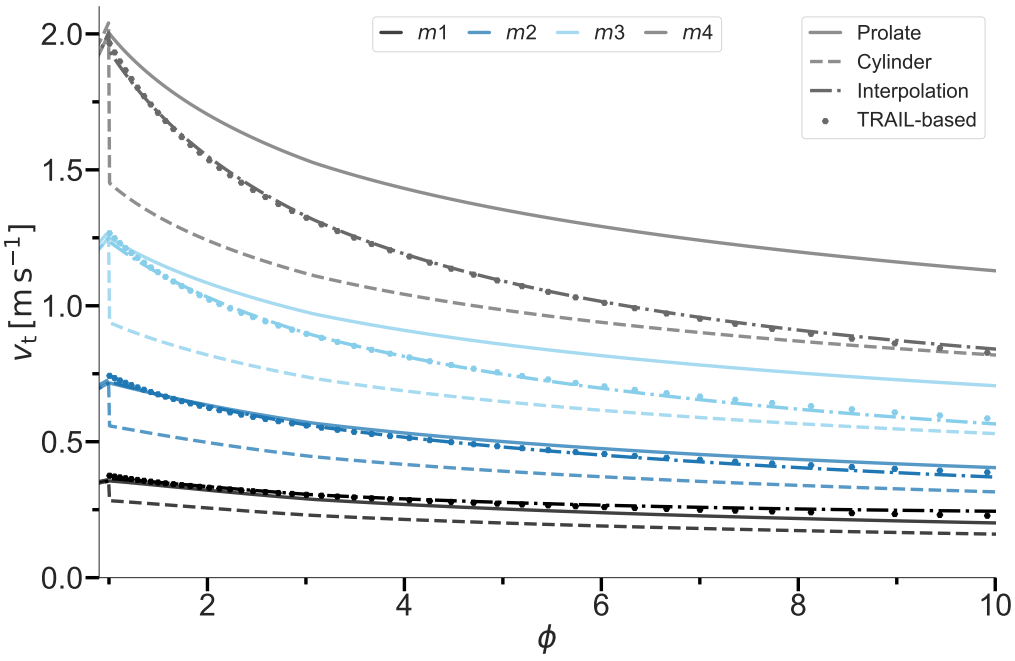

Figure 3. Terminal fall speed v_t dependency on the aspect ratio ϕ for particles with different mass (color-coded), treated as a prolate (solid) or a cylindrical spheroid (dashed), for TRAIL-based data (points), and for an interpolated approach (dash-dotted line, Eq. 31).

advocate an interpolation between the two fall velocities v_{pro} and v_{cyl} using the form

$$v(\phi) = f(\phi)\, v_{\mathrm{pro}} + (1 - f(\phi))\; v_{\mathrm{cyl}}, \tag{31}$$

$$f(\phi) = \beta(m)\, e^{-\alpha(m)\,\phi} \tag{32}$$

This function helps to account for the relatively steep decrease in v_t with increasing ϕ, while matching the asymptotic behavior for the cylindrical approach. We propose a simple fit for the mass dependence of $\alpha(m)$ and $\beta(m)$

$$\begin{aligned} g(m) &= a\, \ln(m) + b, \\ a_\alpha &= 8.60 \times 10^{-2}, \qquad b_\alpha = 1.722\ , \\ a_\beta &= 3.08 \times 10^{-2}, \qquad b_\beta = 1.691\ . \end{aligned} \tag{33}$$

Figure 3 already includes the interpolated fall speed as dash-dotted lines that match the TRAIL results. The interpolation overcomes the need to choose between cylinder and prolate geometry, providing a smooth transition from prolate to cylinder-like behavior of ice columns.

3.2 Response to atmospheric conditions

The terminal fall velocity and the collision efficiency of Böhm are derived from using the Reynolds and Best numbers. This introduces a dependency on atmospheric conditions since both numbers depend on the air density ρ_a and the temperature via the dynamic viscosity $\mu(T)$ (Eqs. A1a & 13). Therefore, v_t and E_c must also change with height if a realistic atmospheric profile is assumed. Pinsky et al. (2001) find an increase in collision efficiency of more than a factor of two for a collision of small droplets ($D_1 \approx 30-50\,\mu$m and $D_2 \approx 10-20\,\mu$m) between the 1000 and 500 hPa levels. The effect of the

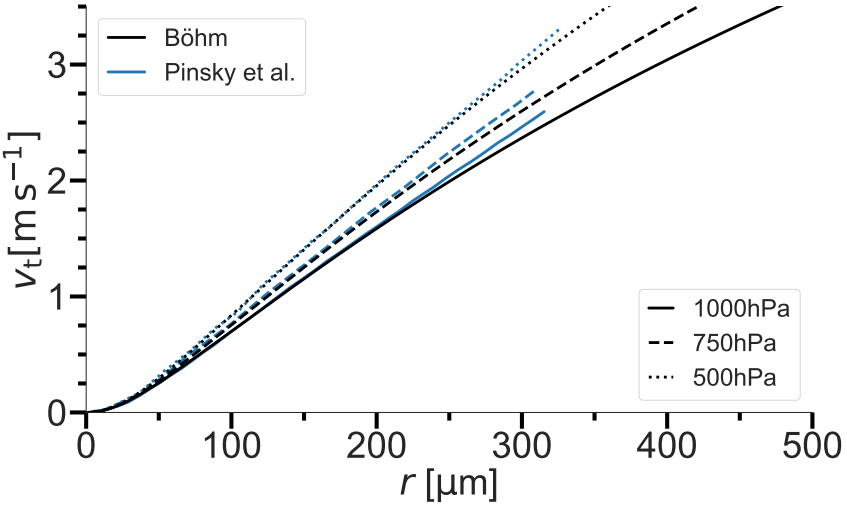

Figure 4. Dependency of v_t on the drop radius for the pressure levels 1000 hPa (solid), 750 hPa (long dashed), 500 hPa (short dashed) for Böhm's scheme (black) and from Pinsky et al. (2001) (blue lines).

atmospheric conditions decreases with increasing droplet size. They argue that 90 % of the enhancement is due to the sensitivity of E_c to the relative velocity difference and only 10 % to an increase in swept volume. Böhm (1992b) finds an increase in E_c with temperature and pressure on the order of only 10 % for small drops ($r_1 \lesssim 30\,\mu$m) and almost no effect for larger ones. Although we expect the work of Böhm to be generalizable, the contradiction of the two results requires an analysis of the dependence of Böhm's fall velocity and collision efficiency parameterizations on different atmospheric states for droplets and ice particles. Compared to Pinsky et al. (2001), we change the surface temperature to freezing point to have a physically justified setup for ice particles at $p = 1000$ hPa. While this change could affect the results, we argue that the exponential decrease in pressure with height dominates the effect over the linear dependence of temperature. Fig. 4 shows the comparison of terminal velocity by droplet size between the results of Pinsky et al. (2001) and with the scheme of Böhm. Böhm's scheme predicts comparable results for all pressure levels. Both results show that the terminal velocity for a drop with $r = 300\,\mu$m is about 25 % greater at 500 hPa than at 1000 hPa. Using the adjustment factor of Beard (1980) allows us to compare the pressure dependence as a function of atmospheric conditions

$$f_{v_t} = \frac{v_t(T,p)}{v_{t,0}(T_0,p_0)} \,, \tag{34}$$

with the reference value of $v_{t,0}$ at $p_0 = 1000$ hPa and $T_0 = 273.15$ K. We look at four different particle types (drop, oblate w. $\phi = 0.25$, prolate w. $\phi = 4$, and graupel w. $\phi = 1$ and $\rho_r = 800\,\mathrm{kg\,m^{-3}}$) and five different masses equal to the mass of a sphere with an equivalent diameter of $D_{eq} = [20, 50, 100, 200, 500]\,\mu$m. In Figure 5 we see that the adjustment factor is proportional to D and can reach a maximum of about 1.3 at 500 hPa for $D = 500\,\mu$m. The difference between particle types is small, but becomes more relevant for larger particles.

In Figure 6 we analyze the effect of the changing thermodynamic state on the collision efficiency for four different collision pairs: drop-drop (D-D, solid lines), graupel-drop (G-D, dash-dotted lines), oblate-oblate (O-O, dashed lines), and prolate-prolate (P-P, dotted lines) collisions. The equivalent diameters of the particles involved are color-

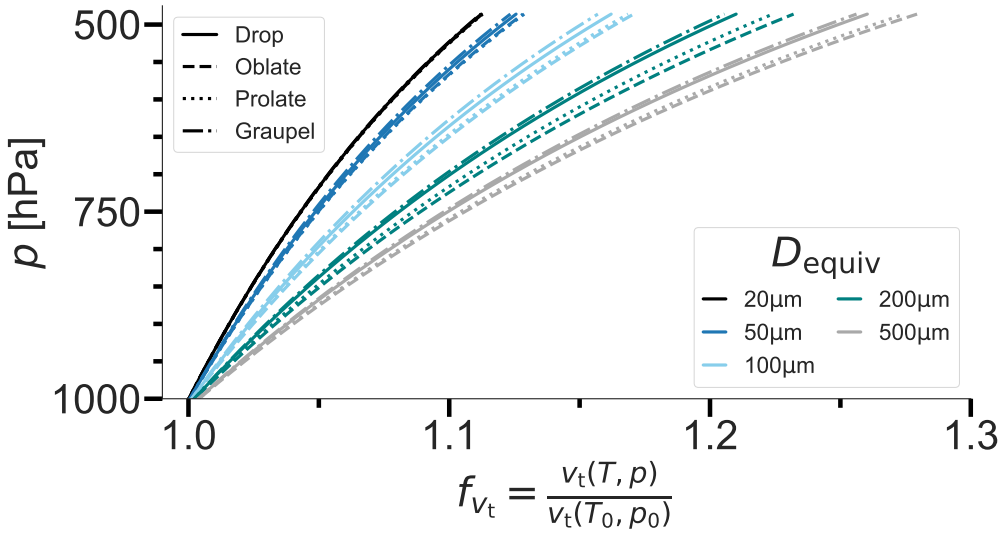

Figure 5. p-profiles of f_{v_t} for drops (solid), oblates (dashed), prolates (dotted), and graupel particles (dash-dotted lines). Color-coded is the equivalent diameter.

coded and include the size range used for the terminal velocity. The impact is inversely proportional to the mass/size and much smaller than for v_t, not exceeding 1.12. We can therefore specify the statement of Pinsky et al. (2001): for small particles, the change in collision efficiency itself dominates the collision behavior. The impact is higher for large particles ($\leq 30\,\%$), where the change in terminal velocity dominates the atmospheric dependence of the collision kernel. Looking at pairs with similar fall velocities, where the collision efficiency rapidly approaches zero, we observe adjustment factors greater than two, as observed by Pinsky et al. (2001) (not shown). The combined effect of atmospheric conditions on terminal velocity and collision efficiency is shown in Figure 7 via the adjustment factor of the collision kernel K. The impact is strongest for the collision of small particles where the onset of effective collision causes strong difference in collision efficiency. For all collisions of larger particles, the total amplification does not exceed 2.5 % and can be considered negligible.

3.3 Habit impact on riming efficiency

While Böhm compares and calibrates his theory for the collision efficiency with results of Schlamp et al. (1975), Martin et al. (1981) and Reinking (1979), more recent results of e.g. Wang and Ji (2000) are available. These are improved with respect to the shape of the particles investigated and the accuracy of the flow field, including unsteady features. Therefore, their results are suitable to evaluate the validity of Böhm (1992a)'s theory for collision events of spheroids with spherical droplets up to radii of $r = 100\,\mu$m. In Figure 8, the analytical collision efficiencies of Böhm are plotted against the simulation of Wang and Ji (2000) for given geometries of oblates, cylinders, and broadly branched crystals. The cylindrical shape is the most difficult to compare due to the mismatch between the actual and spheroidal shape, combined with the asymmetry of the flow.

The results for the oblates are in good agreement with respect to the onset, maxima and cut-offs of all eight particles (Fig. 8a). The direct comparison for the cylinder (Fig. 8b) shows a slightly delayed onset and higher maxima for curves following the theory of Böhm. The cut-offs are shifted to higher collected droplet radii compared to Wang and Ji (2000). Note that terminal velocity interpolation is applied. For branched crys-

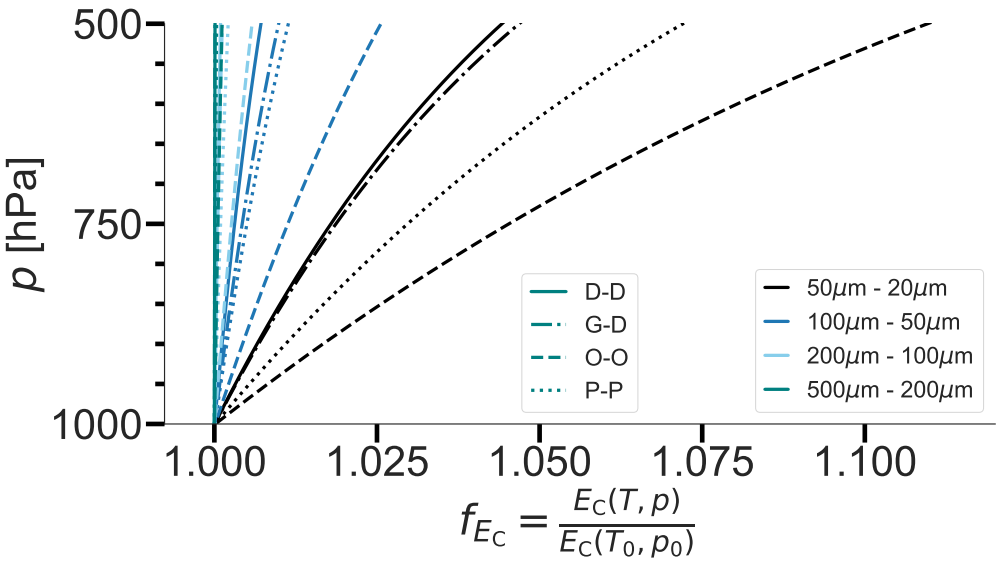

Figure 6. p-profiles of f_{E_c} for a drop-drop (D-D, solid), graupel-droplet (G-D, dash-dotted lines), an oblate-oblate (O-O, dashed), and a prolate-prolate collision (P-P, dotted). Color-coded is the equivalent diameter of the colliding particles.

tals (Fig. 8c) the onset and maximum are quite close. Only the cut-off radii differ, especially for larger crystals. Nevertheless, the overall similarity of the results is satisfactory considering the theoretical assumptions. We conclude that the theory of Böhm provides a suitable framework for parameterizing the collision efficiency of primary habits compared to numerical simulations.

4 Revision of Theory

4.1 Shape-dependent ventilation

Several studies present formulations for habit-specific ventilation coefficients based on the underlying geometry, which may differ substantially from Hall and Pruppacher (1976, HP76) (Prolate: Wang and Ji (2000, WJ00), Ke et al. (2018, Ke18), Kiwitt et al. (2022, K22), Y. Chen et al. (2021), Oblates: Pitter et al. (1974, P74), Ji and Wang (1999, J99), Wang (2021, W21), Nettesheim and Wang (2018, NW17) , spheres: Woo and Hamielec (1971, WH71), Whitaker (1972)).

The left side of Figure 9 shows a collection of these data sets as well as three proposed fits of the dependence of ventilation on X_v for spheres (Hall & Pruppacher, 1976, solid), dendrites (Nettesheim & Wang, 2018, NW17, long dashed), and columns (Ji & Wang, 1999, JW99, short dashed). The formulation of Hall and Pruppacher (1976) shows reasonable behavior for (nearly) spherical particles, but especially for prolate particles, large underestimations of the ventilation coefficient are given (up to 3 for a given X_v). Using the collected data set, we modify the formulation of Hall and Pruppacher (1976, cf. Eq. 30) by adding a ϕ-dependent term to the ventilation coefficient

$$\begin{aligned} f_{\mathrm{v,prolate}} &= f_\mathrm{v} + c_1\, X_{\mathrm{v,equiv}}\quad \phi, \qquad \text{for } \phi > 1, \quad c_1 = 2.8 \times 10^{-2}\ , \\ f_{\mathrm{v,oblate}} &= f_\mathrm{v} + c_2\, X_{\mathrm{v,equiv}}^{3/2}\quad \phi^{-1}, \qquad \text{for } \phi < 1, \quad c_2 = 2.8 \times 10^{-3}\ . \end{aligned} \tag{35}$$

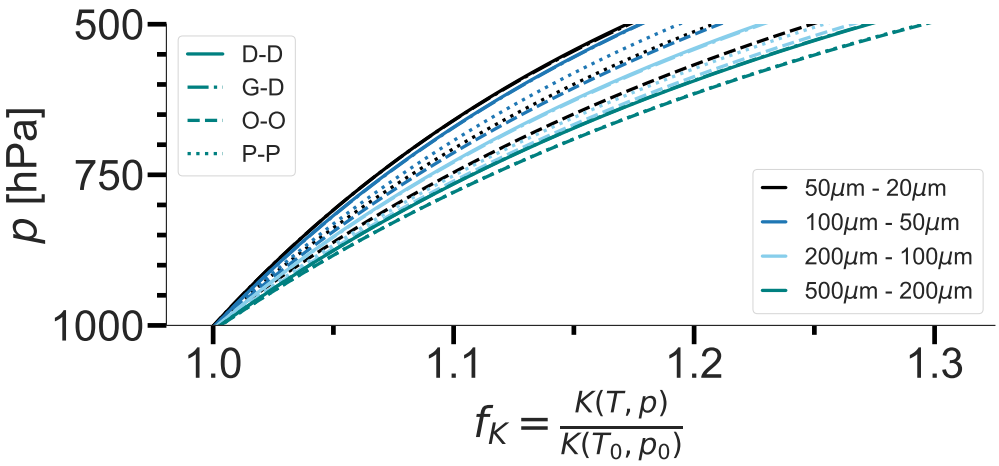

Figure 7. p-profiles of f_K for a drop-drop (D-D, solid), graupel-droplet (G-D, dash-dotted lines), an oblate-oblate (O-O, dashed), and a prolate-prolate collision (P-P, dotted). Color-coded is the equivalent diameter of the colliding particles.

Good agreement with the data can be found for all geometries (right side of Figure 9). It is important to note that we have not introduced any feedback between this shape-dependent (overall) ventilation coefficient (Eq. 9) and the effect of ventilation on the inherent growth function (Eq. 15). The latter only uses the generalized form of Hall and Pruppacher (1976) and considers the habit effect individually.

4.2 Inherent Growth Function

The IGF, as introduced by CL94, can describe primary and secondary habit development in the spheroidal framework (e.g. Jensen & Harrington, 2015; Sulia & Harrington, 2011; Shima et al., 2020)). While providing a fundamental physical description of the growth ratio of the a- to c-axis, the original fit of observational and laboratory results has some inconsistencies when compared with more recent laboratory (Connolly et al., 2012) or modeling studies (Sheridan et al., 2009; Hashino & Tripoli, 2007) for certain temperature regimes.

In this section, we will evaluate the results using the original IGF, point out its deficiencies, and propose another version of the IGF based on observational evidence that corrects some of the shortcomings.

4.2.1 Original version of Chen & Lamb

Takahashi et al. (1991, TH91) provide a set of laboratory measurements that quantify the depositional growth of ice crystals at constant temperature ($T \in [250\,\mathrm{K} - 270\,\mathrm{K}]$) and water saturation. Because of the high quality measurements of the mass, density, and geometry of individual ice crystals, J.-P. Chen and Lamb (1994b) use the TH91 experiments as a benchmark to validate their habit prediction scheme. Figure 10 reproduces Figures 7-9 of J.-P. Chen and Lamb (1994b) using results from the HP scheme without (black) and with the new habit-dependent ventilation coefficient (green lines). It also includes the result with a diagnostic geometry for monomers using the empirical m-D relationship of Mitchell (1996) for aggregates of side planes, columns, and bullets (S3, long dashed lines) and a strictly spherical geometry (short dashed lines). In the lab experiment, the particles freeze from a droplet distribution and the size/weight shows

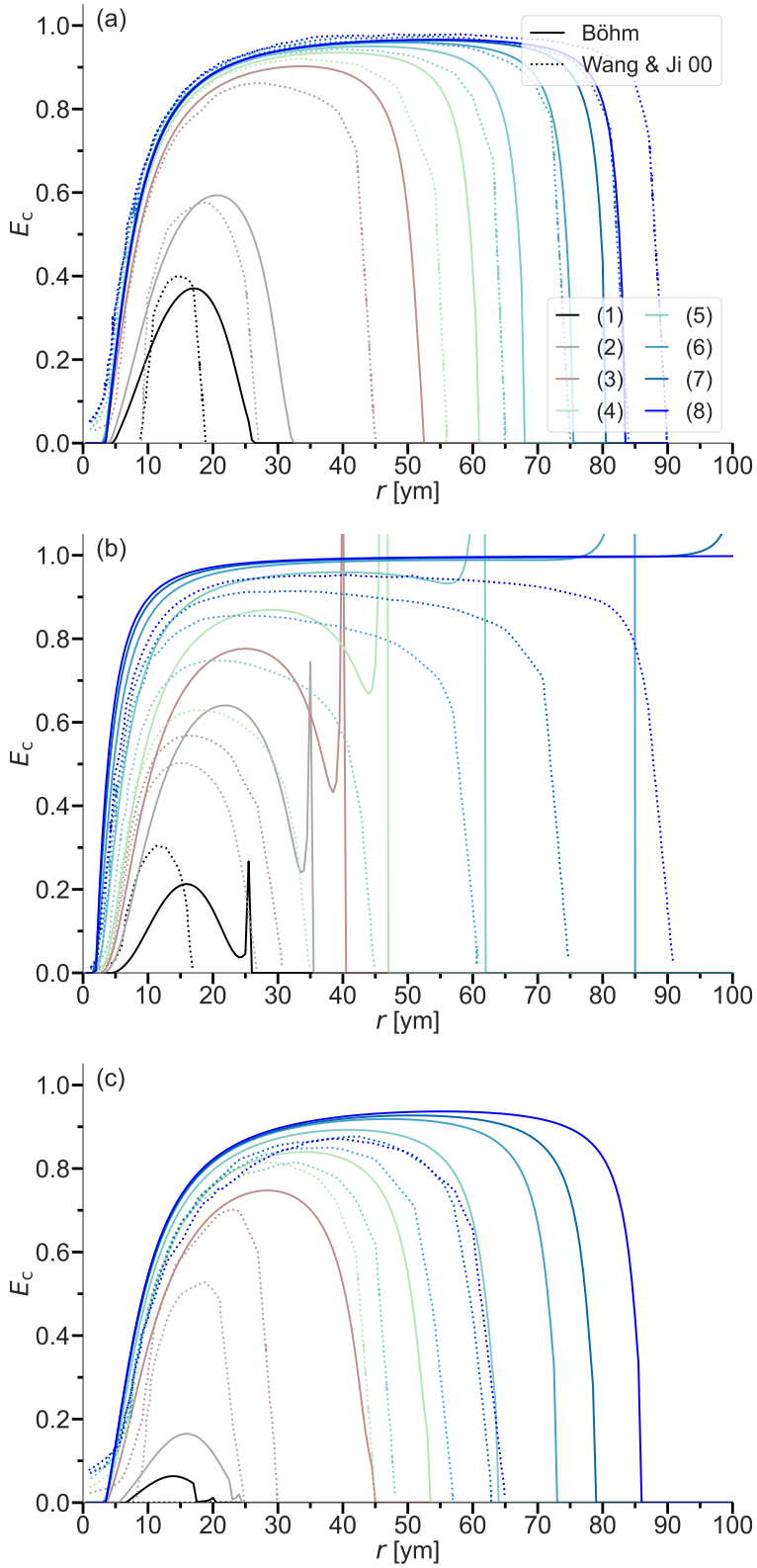

Figure 8. Collision efficiencies of a) thin oblates, b) cylinders, and c) broadly branched crystals with spheres. Particle dimensions and reference numerical simulations of Wang and Ji (2000).

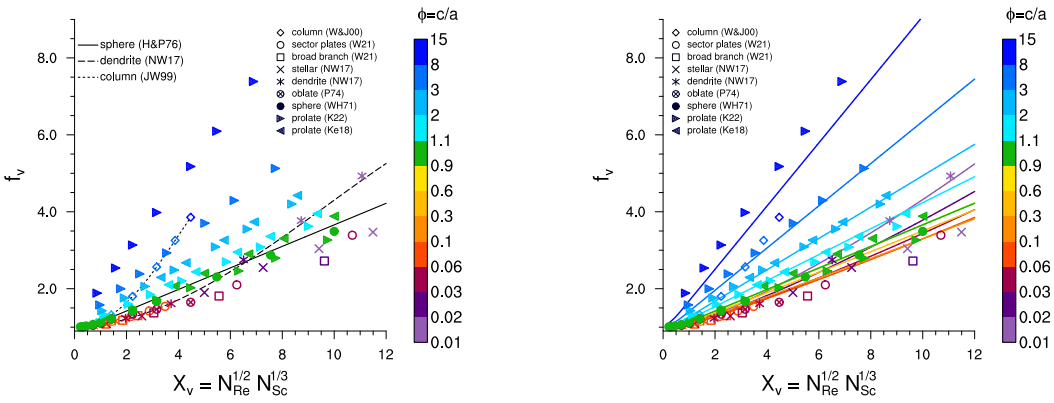

Figure 9. Left: Data points and functional dependencies of $f_\mathrm{v}(X_\mathrm{v})$ for several studies. Right: Proposed functional habit-dependent description $f_\mathrm{v}(\phi)$. The aspect ratio of the assumed particles is color-coded.

slight variations. In the simulations, an initial radius similar to the maximum of the droplet distribution of $r_\mathrm{start} = 2\,\mu$m (Takahashi & Fukuta, 1988) shows overall good agreement with the laboratory data and compares significantly better than the m-D-relationship of Mitchell. The difference in the initial radius is considered small compared to the uncertainties of the measurements and the model assumptions.

For the limiting case of spherical development at $\Gamma = 1$ for temperatures $T \in [253\,\mathrm{K}, 263\,\mathrm{K}]$, the habit prediction is in agreement with the results for spherical particles, and the laboratory results show slightly lighter crystals. In the columnar regime, $T \in [248\,\mathrm{K} - 252\,\mathrm{K}]$ (cold) and $T \in [263\,\mathrm{K} - 268\,\mathrm{K}]$ (warm), the prolates are heavier. For the oblate maximum around $T = 258\,\mathrm{K}$ they are lighter than laboratory data suggest. Since $X_\mathrm{v,equiv}$ does not exceed 1.5 for all particles studied, we see only a slight enhancement of the deposited mass for all non-spherical growth regimes when the habit-dependent ventilation coefficient is included. As expected, prolates are more influenced than oblates, but not enough to change the geometry or density significantly (Fig. 10b&c). From here on, all results will include the habit-dependent ventilation coefficient.

The differences between our model and the laboratory data for particle mass are due to the predicted geometry, too high/low apparent density, or a combination of both. Therefore, Figure 10 (b) and (c) show that within the warm columnar regime, prolates tend to grow to larger aspect ratios than suggested by the laboratory data. Nevertheless, the eventual hollowing captured by the deposition density parameterization is representative. The axis length of oblate growing particles follows the results for the a axis, while showing an inability to represent strongly branched, thin dendritic crystals. This feature is due to the spheroidal assumption and the initial spherical growth up to $D \geq 10\,\mu$m, leading to an overestimation of the c axis size.

If all particles were allowed to grow habit-specifically immediately after nucleation it would reduce the differences observed for the oblate geometry, but leads to unnatural aspect ratios in the columnar regime. The coupling of IGF and deposition density leads to branching for the entire oblate regime and does not reproduce the sharp density minimum for branching particles observed by TH91.

Particles within the cold columnar regime ($T < 253\,\mathrm{K}$) evolve prolate features with a secondary maximum, while TH91 observe nearly spherical or only slightly prolate particles. The habit description becomes ambiguous for the temperature range due to the increased occurrence of polycrystals (based on field observations e.g. Um et al. (2015)). The complex shape of polycrystals and their density cannot be adequately captured by the spheroidal approach. However, model agreement with laboratory data on ice mass deposition is improved by the explicit habit prediction and habit-dependent ventilation.

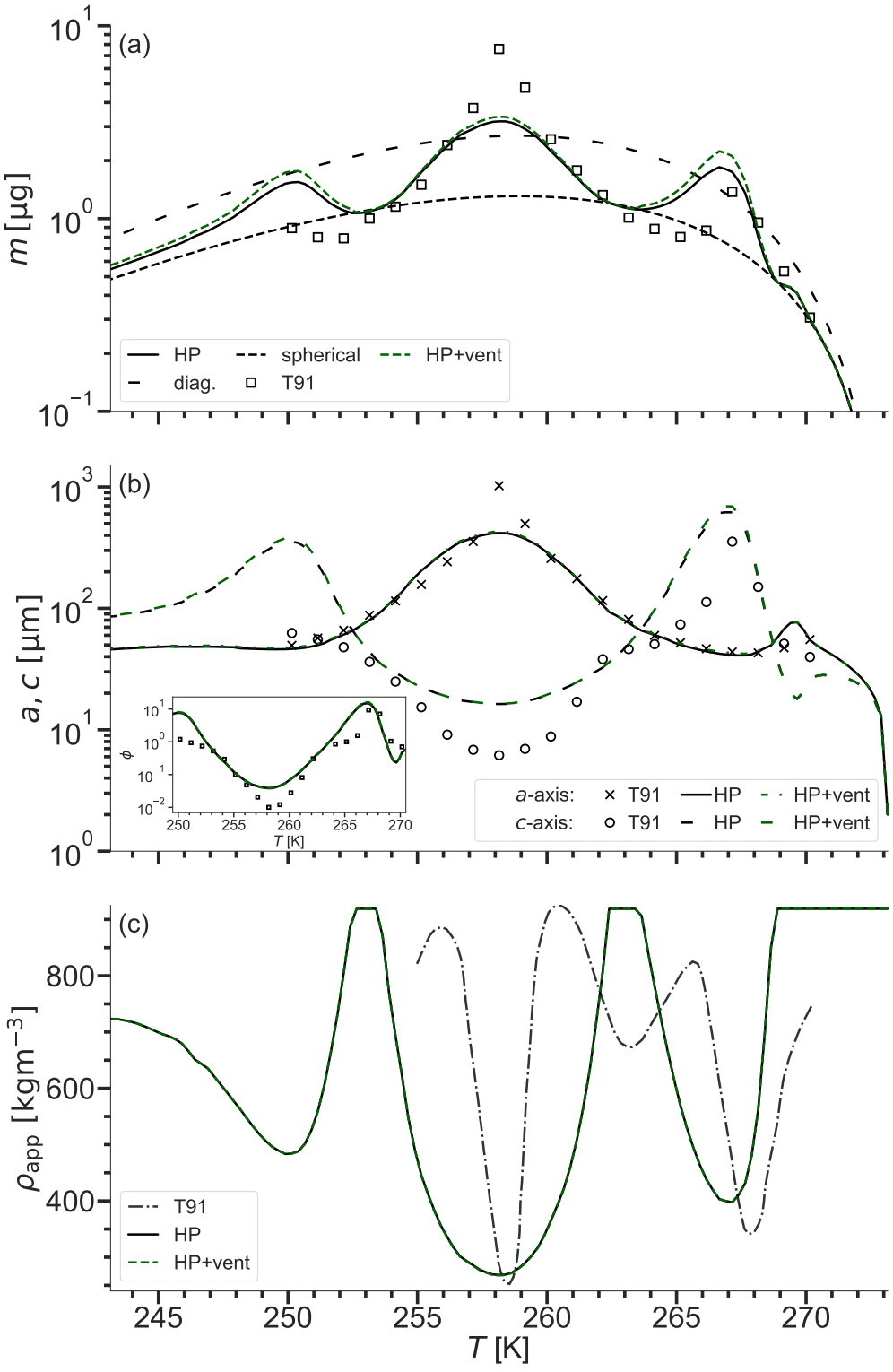

Figure 10. T-dependence of (a) m, (b) geometry ($a-, c-$axis, ϕ), and (c) $\rho_{\mathbf{app}}$ after 10 min of vapor deposition. The black line shows results for the baseline HP, green lines include the habit-dependent ventilation coefficient, and the markers show results of Takahashi et al. (1991, TH91). (a) includes a line for a particle with a diagnostic geometry (diag., long dashed) and that for a spherical crystal (short dashed).

4.2.2 Polarimetric signal of model results

To further analyze the modeled results, we use the methods proposed by Myagkov, Seifert, Wandinger, et al. (2016) to calculate the polarizability ratio for the different temperature regimes. Myagkov, Seifert, Bauer-Pfundstein, and Wandinger (2016) combines the methods of Melnikov and Straka (2013) and Matrosov et al. (2012) to obtain the polarizability ratio ρ_e (PR) from a 35 GHz cloud radar with a hybrid polarimetric configuration. The PR is based on the particle shape and its dielectric properties and can be used to retrieve information about the environmental conditions under which particles develop certain habits and apparent densities. For their analysis, only particles near cloud top are considered since these observed characteristics developed in local conditions and particle mixtures are unlikely. Myagkov, Seifert, Wandinger, et al. (2016) show that observed PRs are similar to those obtained from the free fall chamber of Takahashi et al. (1991) within the uncertainties of the (temperature) measurements. The PR analysis provides insight into the functional coupling between geometry and density via the IGF (Eq. 7). It is important to note that the sensitivity of the PR to a change in geometry is higher for high particle densities (see Fig. 2 of Myagkov, Seifert, Wandinger, et al. (2016)).

Figure 11 compares the PRs of TH91 (open grey triangles, all growth times), observations near cloud tops (Myagkov, Seifert, Wandinger, et al., 2016, black squares), and the results after three and ten minutes of simulated growth with HP (pluses/circles, color indicates app. density). We show two different time steps of *McSnow* to distinguish between primary and secondary habit effects of oblates: after three minutes, only primary habits develop, so that particles reach a maximum PR before branching. The qualitative results of the HP compare well with TH91 and observations. Particles with the most extreme PRs do not develop in *McSnow*, and their transition between regimes appears to be shifted.

For the maximum in the warm prolate regime, the particles appear to have the correct aspect ratio (Fig. 10(b)) with a slightly lower PR than the observations. This finding suggests that the warm prolate maximum of the IGF may cause excessive hollowing. In addition, the maximum may be too broad, causing an offset in the transition regime.

Oblates that turn out not to be thin enough (cf. Fig. 10b)) result in a PR that (after three minutes) is not as low as suggested by the observations, but is qualitatively consistent. The strong branching of the particles throughout the oblate-favoring regime leads to an overestimated reduction of the PR for the simulated particles. According to this analysis, it seems necessary to postpone branching to later stages of particle evolution.

Warm oblates ($269 < T < 273\,\mathrm{K}$) and the cold prolate maximum ($T < 252\,\mathrm{K}$) cannot be fully evaluated due to a lack of observational data points. However, existing laboratory measurements suggest that these maxima may be overestimated. The above deficiencies for the specific regimes are:

1. oblate minimum around $T = 269\,\mathrm{K}$ is too low,
2. prolate maximum around $T = 267\,\mathrm{K}$ too high m with too low ρ_{app},
3. crystals around $T = 258\,\mathrm{K}$ not thin enough ,
4. cold prolate/polycrystal regime exhibits has too high m and ϕ.

4.2.3 Updated Inherent Growth Function

To overcome the above deficiencies, we propose a modification of the IGF and related assumptions to improve the habit-dependent particle growth. Starting from point one, there is no clear evidence for a strong oblate minimum at $T = 269\,\mathrm{K}$, either from the observations shown above or from other sources such as Bailey and Hallett (2009). We therefore use the values suggested by Sei and Gonda (1989). Future retrievals may be useful to evaluate this change.

Point two can be addressed by reducing the IGF maximum around $T = 267\,\mathrm{K}$ by 25% and fitting the curve to $\Gamma = 1$ at the appropriate temperatures. This change should

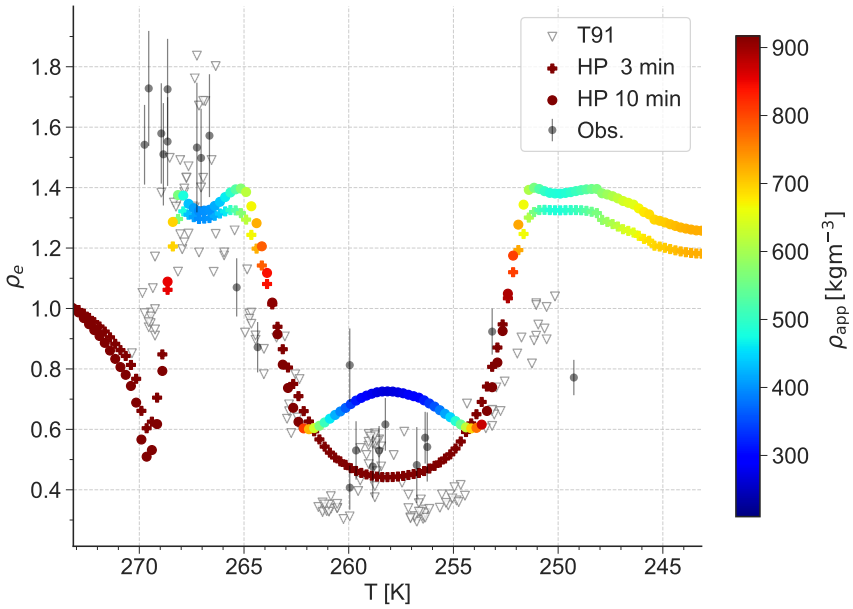

Figure 11. T-dependence of polarizability ratios ρ_e for ice crystals grown in the free-fall chamber (open grey triangles), with HP ([+] for $t = 3\,\text{min}$, [•] for $t = 10\,\text{min}$), and observed near cloud tops (black squares, error bars represent ±1 standard deviation). Color-coded is the particle's apparent density ρ_{app}.

result in slightly shorter, lighter, but denser columns that better match the TH91 data. For PR, the geometric change is (partially) offset by an increase in density.

In the oblate growth regime, the IGF initially produces the correct geometries (cf. 3 min results), but branching seems to occur too early and for a relatively wide range of planar particles. Comparing the simulated density with the wind tunnel results (Fig. 10c), we see that particles branch only for a narrow temperature range. So instead of changing the IGF, we change the branching criterion to better resemble the onset of branching. In the formulation of JH15, branching does not occur before $a \geq 100\,\mu\text{m}$. Here, we assume that particles branch when $a \geq 200\,\mu\text{m}$, effectively delaying the onset of branching.

For the final point, we merge the time-dependent growth rates of TH91 (Tab. 2 of Takahashi et al., 1991) with the results of Sheridan (2008) and Sheridan et al. (2009). Connolly et al. (2012) also report a discrepancy between observed and modeled crystals for the regime around $T = 253\,\text{K}$ using CL94's IGF, but they assume oblate growth for colder temperatures. Due to the dominance of polycrystals, it becomes difficult to generalize these habits to either prolate or oblate spheroids. The advantage of assumed columnar growth is the immediate hollowing, which effectively reduces the apparent density, whereas if oblate growth is assumed, the branching criterion of JH15 is not met because the particles remain nearly spherical.

Figure 12 shows the original IGF (black) and our proposed version (blue line) combining the above modifications, together with the diagnosed Inherent Growth Ratios of Takahashi et al. (1991) (red and black dots). In Figure 13, results of the depositional growth experiment using the new IGF (blue lines) are compared with the original results (black lines) for mass, axis measure, and apparent density. Using the new IGF, the accumu-

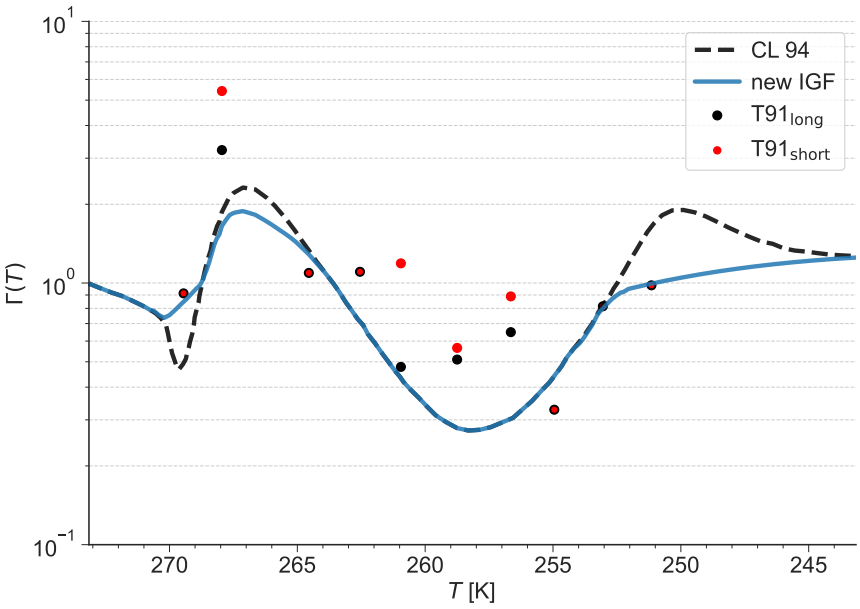

Figure 12. Inherent Growth Function of CL94 and our new formulation as a function of temperature. Explicit values of Takahashi et al. (1991) are marked as red and black dots.

lated mass is decreased for the warm prolate peak as well as in the polycrystalline regime, removing the secondary peak (colder $T = 253\,\mathrm{K}$) (Fig. 13a). In terms of geometry, the changes induced by the modified IGF are suitable for both prolate regimes. There is no modification of the IGF in the oblate regime around $T = 258\,\mathrm{K}$. The reduction of the warm oblate ϕ minimum is in good agreement with the laboratory results. The resulting changes in particle density are negligible.

A second experiment includes the modified IGF, combined with the modified branching criterion of $a \geq 200\,\mu\mathrm{m}$ introduced above (IGF2+, red lines). The lower limit of $D > 10\,\mu\mathrm{m}$ for habit development can be physically justified by the studies mentioned above, but at the same time it prevents the development of very thin oblates observed by Takahashi et al. (1991). In this setup we therefore remove the limiter and allow free evolution after nucleation, which gives the best agreement with TH91. The modifications result in more mass being deposited around $T = 258\,\mathrm{K}$, bringing the results closer to the TH91 measurements. In terms of geometry, the transition from the oblate to the polycrystalline regime as well as the shape of the oblates are very similar to the measurements. The coupling of the IGF and the deposition density leads to subsequent changes in the apparent density. It seems difficult to assess the change in apparent density, but the narrowed oblate minimum seems justified, while the warm prolate minimum might overestimate the particle density. To evaluate the combined effect of shape and density, we analyze the PR with the updated IGF including the additional modifications. Figure 14 confirms that this setup can remove the major deficiencies between the laboratory measurements and the simulation. The warm oblate regime shows higher PRs, while the warm prolate maximum is slightly closer to the majority of observational data due to the interplay of geometry and density (less hollowing). Nevertheless, the highest PRs cannot be matched. This discrepancy can be attributed to the parameterization of the hollowing, since the AR is well matched. In the cold oblate regime, delayed branching signif-

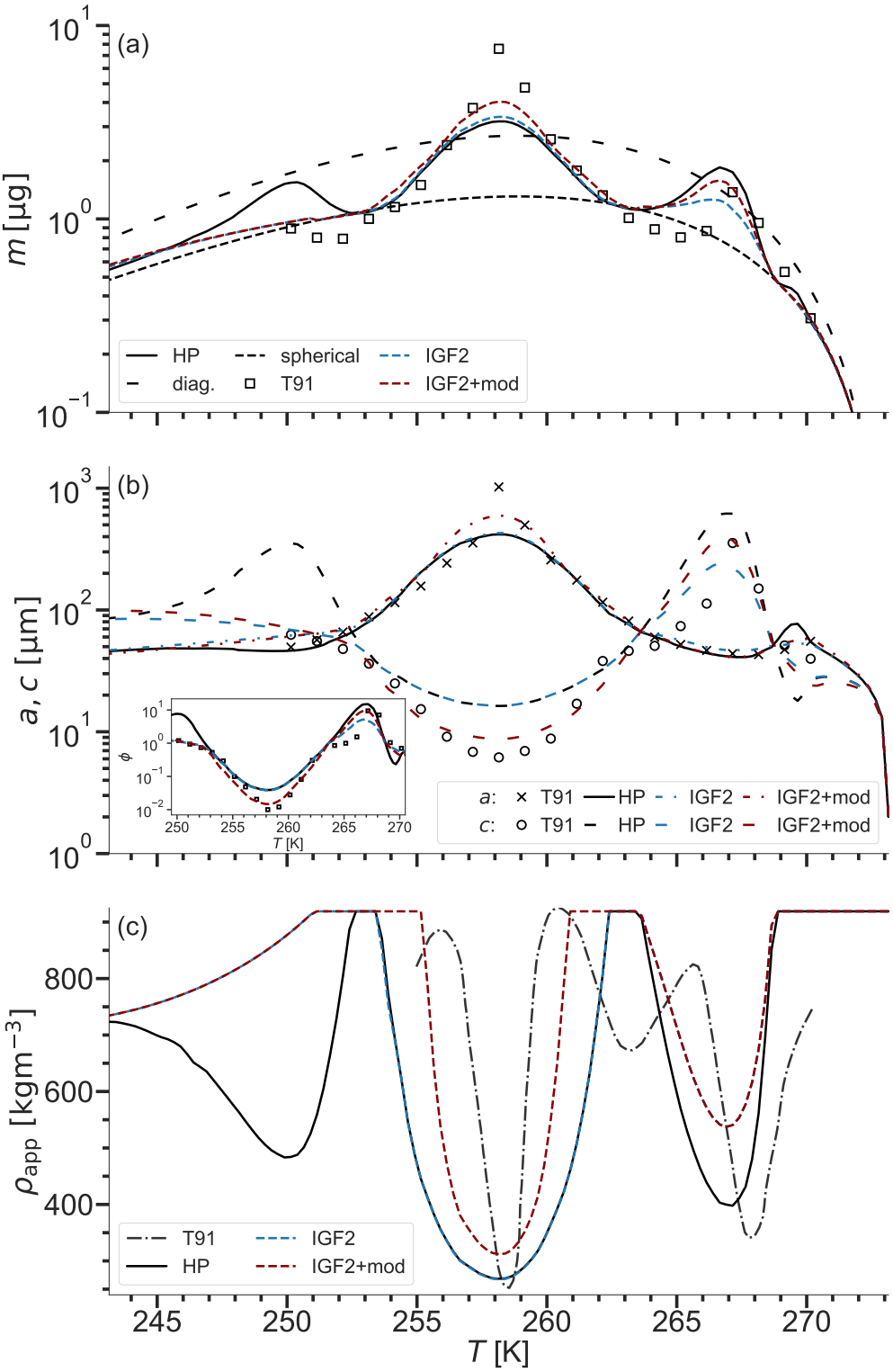

Figure 13. As Fig. 10 but also compared with the results of the updated IGF (blue) and of the updated IGF including branching modification (IGF2+, red).

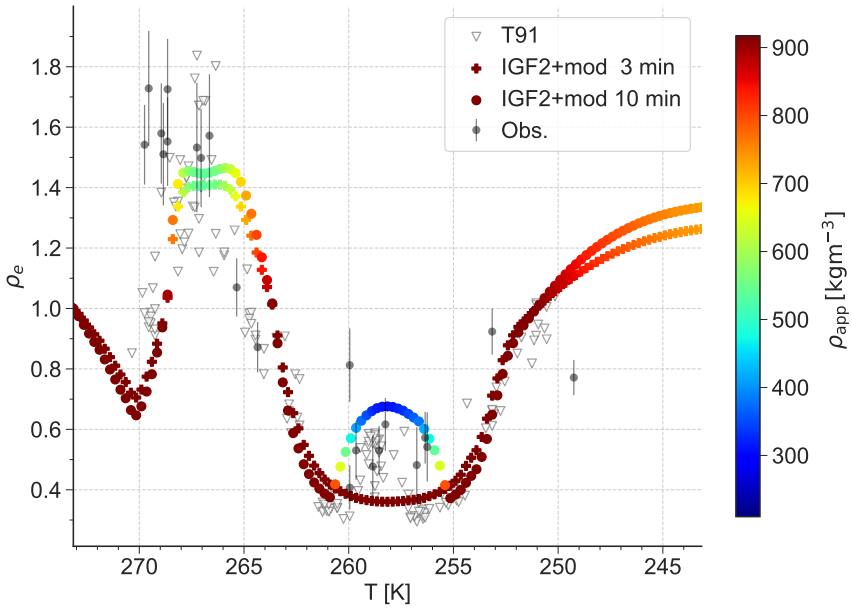

Figure 14. As Fig. 11 but with the new IGF and altered branching criterion.

icantly improves the agreement of the PR with the observational and T91 results. The evolution of particles with very low PRs ($\rho_e < 0.4$) can be observed after three minutes, as suggested by the measurements. The same is true for the increase in PR due to strong branching around $T = 258\,\mathrm{K}$. Finally, the transition from oblate to polycrystals seems to agree better with the results of T91 and Myagkov, Seifert, Wandinger, et al. (2016). For possible further modifications of this version of the IGF, more retrieved observational or laboratory data are needed. In particular, the regimes that are sparsely populated by measurements (such as the polycrystalline region) could be of great benefit to such a detrimental function as the IGF.

5 Case study exhibiting sensitivities

Habit prediction has a pronounced impact on many microphysical processes and can introduce variability among particles by abandoning static m-D and v_t-relations. *Mc-Snow* is unique in the sense that it combines the habit prediction scheme of J.-P. Chen and Lamb (1994b) and Jensen and Harrington (2015) with the full set of parameterizations of Böhm. Using Böhm's framework for the parameterization of particle properties allows a physically consistent and mathematically continuous description of the habit dependency of most microphysical processes. The effect of habit prediction on particles at constant temperature has been shown in Figure 10, but this setup can only serve as a limiting case. In real clouds, hydrometeors experience different thermodynamic conditions and change the conditions themselves by absorbing/releasing water and latent heat. We soften the constraints implied by the laboratory setting by focusing on a setup where particles fall through a one-dimensional column (rain/snow shaft) with a prescribed atmospheric profile. The model setup (Fig. 15) is defined to mimic different sections inside a cloud where certain relevant ice-microphysical processes dominate. In the upper part, depositional growth of small particles should govern the evolution. The ice mass

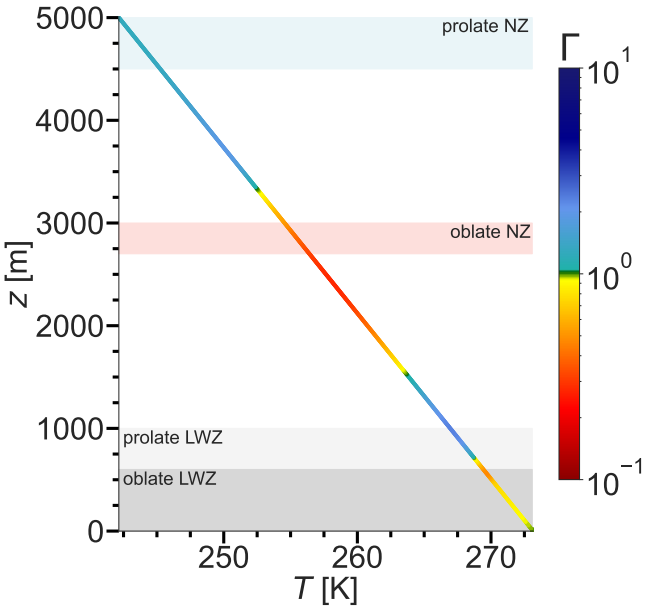

Figure 15. Background atmosphere for the 1-D model simulations incl. the vertical profiles of temperature and corresponding IGF. The nucleation (NZ) and liquid water zones (LWZ) are situated in the shaded regions for the respective cases.

accumulated by deposition changes the shape and fall velocity. Both terminal velocity and geometry are linked to the likelihood of collision events and change the onset of aggregation and how effective it is. In the lower part of the profile, both monomers and aggregates encounter a liquid water zone (LWZ) where the impact of the ice habit on the effectiveness of riming is examined.

5.1 Setup

Similar as in Brdar and Seifert (2018), the temperature profile is constructed using the surface temperature of $T_{\text{surf}} = 273\,\text{K}$ and a constant lapse rate of $\gamma = 0.0062\,\text{Km}^{-1}$. The domain height is case specific with $z_{\text{top}} = 5000\,\text{m}$ ($T_{\text{top}} = 242\,\text{K}$) for a prolate and $z_{\text{top}} = 3000\,\text{m}$ ($T_{\text{top}} = 254.4\,\text{K}$) for an oblate favoring regime. Water vapor, liquid water, and temperature are assumed to be constant and not increased or decreased by any microphysical process.

In the upper 80 % of the (case-specific) domain, particles grow solely by vapor depositional growth and aggregation at a supersaturation of 5 %. In the lower 20 %, the regime is dominated by riming due to a liquid water zone ($LWC = 0.2\,\text{gm}^{-3}$), which enhances particle growth and in turn increases the probability of aggregation. We do not impose a subsaturated regime because the habit-specific effect is small and possible aggregation events become unlikely due to decreasing particle size. The initial properties (mass and size) of the ice crystals are drawn from a gamma distribution with a mean mass equal to the mass of a spherical ice particle with a diameter of $D = 10\,\mu m$, the initial aspect ratio is set to $phi = 1$. Particles are generated at a constant nucleation rate within a nucleation zone that spans 10 % of the total domain height. A random initialization height has a positive effect on the variance of the developed particle habits due to the different atmospheric conditions compared to constant nucleation at the domain top. Particles larger than $D > 10\,\mu m$ are initialized with a density derived from

empirical mass-area relations to avoid underestimating the actual particle geometry and overestimating the fall velocity.

We integrate the model over 10 h to reach a steady state, and all statistical quantities are averaged over the last 5 h. Riming is treated by the stochastic riming scheme (cf. Brdar & Seifert, 2018; Bringi et al., 2020) which makes use of the theory of Böhm for terminal velocity and collision efficiency.

Sheridan et al. (2009) shows that habit development is strongly controlled by conditions shortly after nucleation, when relative changes in mass and shape are most pronounced. Numerical models of the atmosphere typically assume uniform thermodynamic conditions within a grid cell. Especially in regions where the IGF shows strong gradients, the uniform treatment leads to different habits as if the actual thermodynamic conditions at the position of the particles were assumed. In Large Eddy Simulation (LES) and Numerical Weather Prediction (NWP) models the vertical spacing inside clouds can easily exceed $\Delta z = 50\,\mathrm{m}$ (Dziekan et al., 2019; Shima et al., 2020), which already results in a temperature difference between the lower and upper edge of the cell of $\Delta T \geq 0.3\,\mathrm{K}$ (assuming the above temperature gradient). Hence, we strongly recommend an interpolation of the atmospheric state to the particle position, making the habit evolution independent of the resolution of the atmospheric grid.

5.2 Deposition

The results in Figure 10 imply a change in deposition rate due to the habit prediction and the preceding dependencies on capacitance, ventilation, and fall velocity. To study the effect of particle habits without the complex feedback between ice microphysical processes, we suppress aggregation and remove the liquid water layer for the time being. We focus on a prolate and an oblate favoring initial growth scenario as archetypes for typically observed monomer cases and show why it is important to consider ice habits.

5.2.1 Prognostic geometry vs. m-D-relationship

Figure 16 illustrates the diversity of particle properties induced by the temperature dependence (original IGF of CL94) of the habit evolution of the mass, velocity, and density of individual crystals relative to their maximum dimension. Since there is no complete set of empirical formulations, we use individual relations for the variables: mass-size of Mitchell (1996), velocity of A. Heymsfield (1972, Tab. 3), and apparent density from Pruppacher and Klett (1997) for comparison.

Unless otherwise stated, we compare the results of the explicit habit prediction with those of simulations using the diagnostic geometry for monomers and aggregates as introduced by Brdar and Seifert (2018) using the power law of Mitchell (1996) for aggregates of side planes, columns, and bullets.

Like Shima et al. (2020), we use the normalized mass of the ice particles

$$\overline{m} = \frac{m}{\rho_\mathrm{i}\,\frac{\pi}{6}\,D^3}\,, \qquad D = 2\,\max(a,c)\;. \tag{36}$$

The terminal velocity has been normalized to surface conditions $v_{\mathrm{t},0}$ to remove the direct atmospheric effect (see Sec. 3.2) and ease comparison with the empirical equations of A. Heymsfield (1972) that assume a reference pressure of $p = 1000\,\mathrm{hPa}$.

The empirical mass-size-relations for aggregates, plates, columns, or broadly branched crystals of M96 may be able to estimate an average behavior of the mass-size spectrum for certain diameter ranges, but the variations caused by local temperature and supersaturation effects seem impossible to describe with prescribed thresholds or a mixture of static relations. Depending on the nucleation conditions prescribed by the initialization height and mass, the particles develop different characteristics for the same maximum dimension. For larger maximum dimensions, we see that the diagnostic geometry of aggregates tends to underestimate the prolate and overestimate the oblate particle mass, demonstrating the weakness of using the diagnostic approach for the differ-

ent regimes. Habit-specific relationships do not significantly improve the agreement, and to use them additional thresholds based on particle properties would have to be defined. This strongly emphasizes the importance of the HP for predicting ice growth in clouds.

Specifically for the mass of prolate particles, a sharp increase around $D = 0.4\,\mathrm{mm}$ can be observed, accompanied by an increase in velocity and apparent density. This behavior cannot be matched by the slope of any empirical relation and exhibits a caveat of the deposition density description for secondary habits as formulated by JH15: the deposition density is generally dependent on the surrounding conditions and is assumed to approach ice density for the transition from prolate-favoring to oblate-favoring conditions (and vice versa) ($\Gamma \to 1 \Rightarrow \rho_{\mathrm{app}} \to \rho_{\mathrm{i}}$, cf. Eq. 7). Because the columns cannot satisfy the branching criterion of JH15, they grow with ice density not only when in regions that mandate spherical growth, but also when falling in oblate-favoring conditions where the addition of high-density mass causes acceleration (Fig. 16(b)). Coupled with the comparatively short residence times in habit-forming regimes due to high fall velocities, columns do not substantially change the habit they initially formed under conditions close to their nucleation height. The deposition density for habits growing in unfavorable conditions is unknown. Comparison with the empirical relation for apparent density suggests that the assumption of secondary habits (immediate onset and subsequent degree of hollowing) may be overstated.

Particles nucleated under oblate-favoring conditions can form relatively small ARs once they begin to branch. The development of a large area presented to the flow increases the drag, leading to an almost constant terminal velocity at large diameters. This feedback positively supports habit development in the prevailing atmospheric conditions. Compared with the empirical relation of the apparent density of dendrites, the onset of branching seems premature and further motivates our changes to the branching criterion. Oblates that fall into conditions of higher deposition density experience an increase in apparent density. It is unclear if this behavior can be physically motivated or is a feature of the coupling between IGF and deposition density. Hashino and Tripoli (2007) hypothesize that dendritic arms grow under prolate-favoring conditions due to an increased ventilation effect along the tips, while there is no current theory for columns. Future laboratory experiments may help to better understand this behavior and motivate a modified treatment of the modeled particles, but for now, we stick with the secondary habit treatment proposed by JH15.

To get a quantitative impression of the average effect of the habit prediction, Figure 17 shows the vertical profiles of mass flux, deposition rate, and mass-weighted terminal velocity $\overline{v}_{\mathrm{t}}$. A comparison of particles following the m-D-relation of aggregates from Mitchell (1996, solid lines) with the original formulation of cylindrical hydrodynamic behavior of Böhm (1992a) (long-dashed, HP) shows that the habit prediction significantly reduces mass flux (precipitation rate, Fig 17a). The diagnostic geometry predicts larger areas for particles of a certain maximum dimension than those of prolate spheroids of the habit prediction. This drastically increases the deposition rate (Fig. 17b) via the increased capacitance, while leading to lower fall velocities for the same mass (Fig. 17c). Slower particles prolong the residence time, leading to even more depositional growth that cannot be compensated for by the increased ventilation effect for the fast columnar particles. In turn, particles that follow the m-D-relationship can develop up to twice the mass flux of particles that develop a habit.

Using the interpolation for the velocity of prolates increases the observed difference and further reduces the mass flux due to the effective acceleration of the particles (see section 3.1). Upcoming results will only use the interpolated fall velocity for prolates due to consistency with laboratory results.

The behavior of particles nucleated under oblate-favoring conditions qualifies the results of the simplified experimental setup of Takahashi et al.: Plates generate more mass than particles with a diagnostic geometry, but the effect is less pronounced than for prolates. Even at higher masses, oblates have a slightly longer residence time than particles without a habit. The development of thin plates or dendritic structures increases

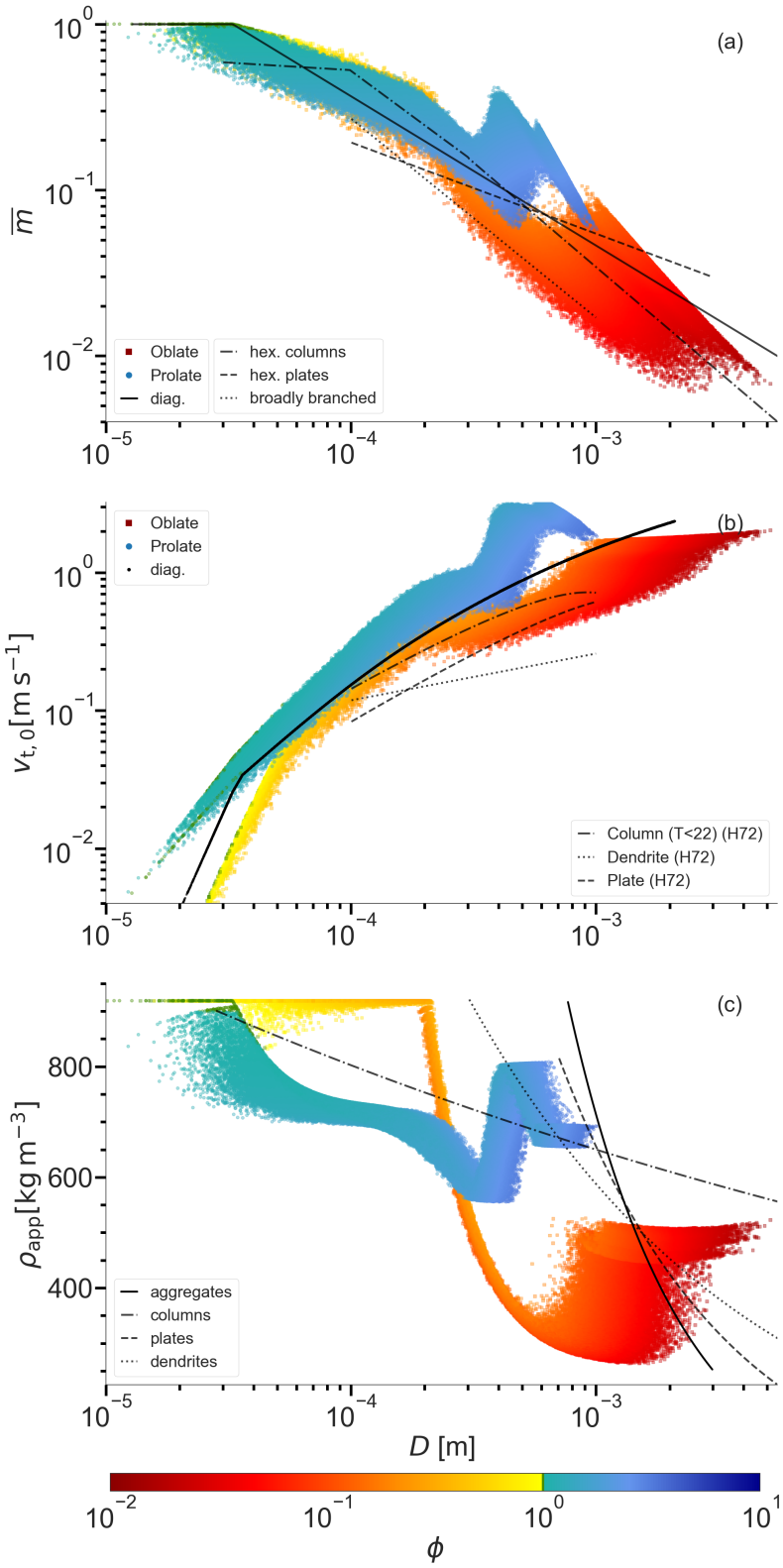

Figure 16. $\overline{m}$-D (a), $v_{t,0}$-D (b), and ρ_{app}-D-relations (c) for the steady state of the simulation. Markers represent the simulations using a diagnostic geometry and an explicit habit prediction. The particles AR ϕ is color-coded. Lines in (a) are empirical relations of Mitchell (1996), in (b) of A. Heymsfield (1972), and in (c) from Pruppacher and Klett (1997).

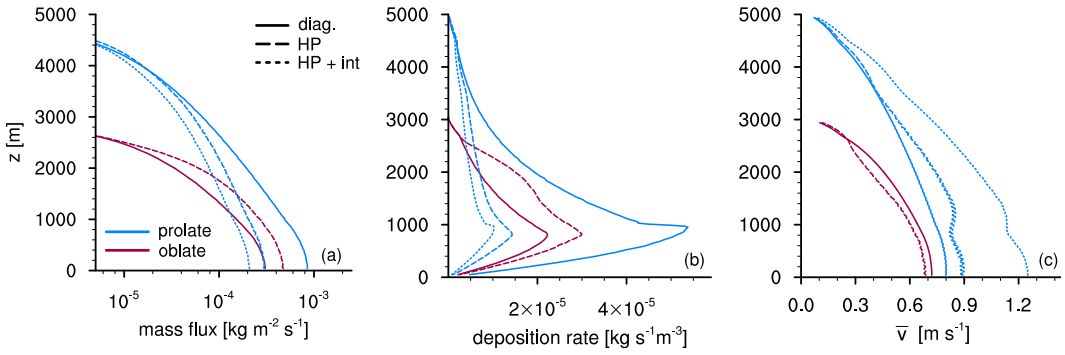

Figure 17. Comparison of vertical profiles of (a) mass flux, (b) deposition rate, and (c) mass-weighted velocity $\overline{v}$ for particles nucleated in a prolate (blue, $\Delta z_{\mathrm{nuc}} = 4500 - 5000\,\mathrm{m}$) and an oblate (red, $\Delta z_{\mathrm{nuc}} = 2700 - 3000\,\mathrm{m}$) regime using a diagnostic geometry (solid), habit prediction with cylinder (dashed), and habit prediction with interpolated velocity for prolates (short-dashed).

the surface area, causing a positive feedback on capacitance and ventilation, amplified by habit-dependent ventilation, increasing the deposition rate.

An opposite effect on the first-order variables of the two categories of habits can be observed: the HP effectively causes an increase in precipitation mass for oblate particles and a decrease for prolate particles (such as the mass flux/precipitation).

5.2.2 Updated IGF

While we do not expect the effect of the updated habit scheme to be nearly as pronounced as in the isolated laboratory setup of Takahashi et al., the changes may initialize altered habit developments. In particular, particles nucleated in the cold prolate regime remain more spherical and are therefore more prone to primary habit change. Figure 18 shows the changes in both growth regimes caused by the modifications of the IGF, including the branching criterion. The flattening of the prolate maximum in the cold regime ($T < 253\,\mathrm{K}$) leads to the evolution of fast falling crystals because their AR remains close to sphericity and their apparent density is comparatively high, improving the agreement with the empirical relation of the apparent density of columns. These crystals short residence times result in reduced total depositional growth and maximum dimension, and ultimately shorter lifetimes as they fall out as precipitation.

The change in branching criterion delays the development of porous structures for plates, and the more compact shape results in an initially increased terminal fall velocity. As soon as strong branching sets in, v_{t} reaches lower velocities as for the original branching criterion closer to the empirical relation for dendrites of A. Heymsfield (1972). The delayed onset of branching agrees well with the empirical relation for the apparent density of dendrites.

Generally, the modifications to the IGF and branching criterion show the desired impact on mass and apparent density while terminal velocities are fairly high.

The average vertical profiles in Figure 19 allow to summarize the quantitative behavior: The mass flux for plates following the original IGF is significantly increased compared to the diagnostic counterpart. For the updated formulation, the mass flux is similar to that of particles without explicit habits. This highlights the importance of the initial growth phase, where the exact onset of branching significantly affects the particle characteristics. The new IGF causes a decrease in mass flux for both the columnar and prolate cases compared to the original IGF configuration for similar reasons: While prolates remain more spherical and less hollow, oblates branch later and the more compact

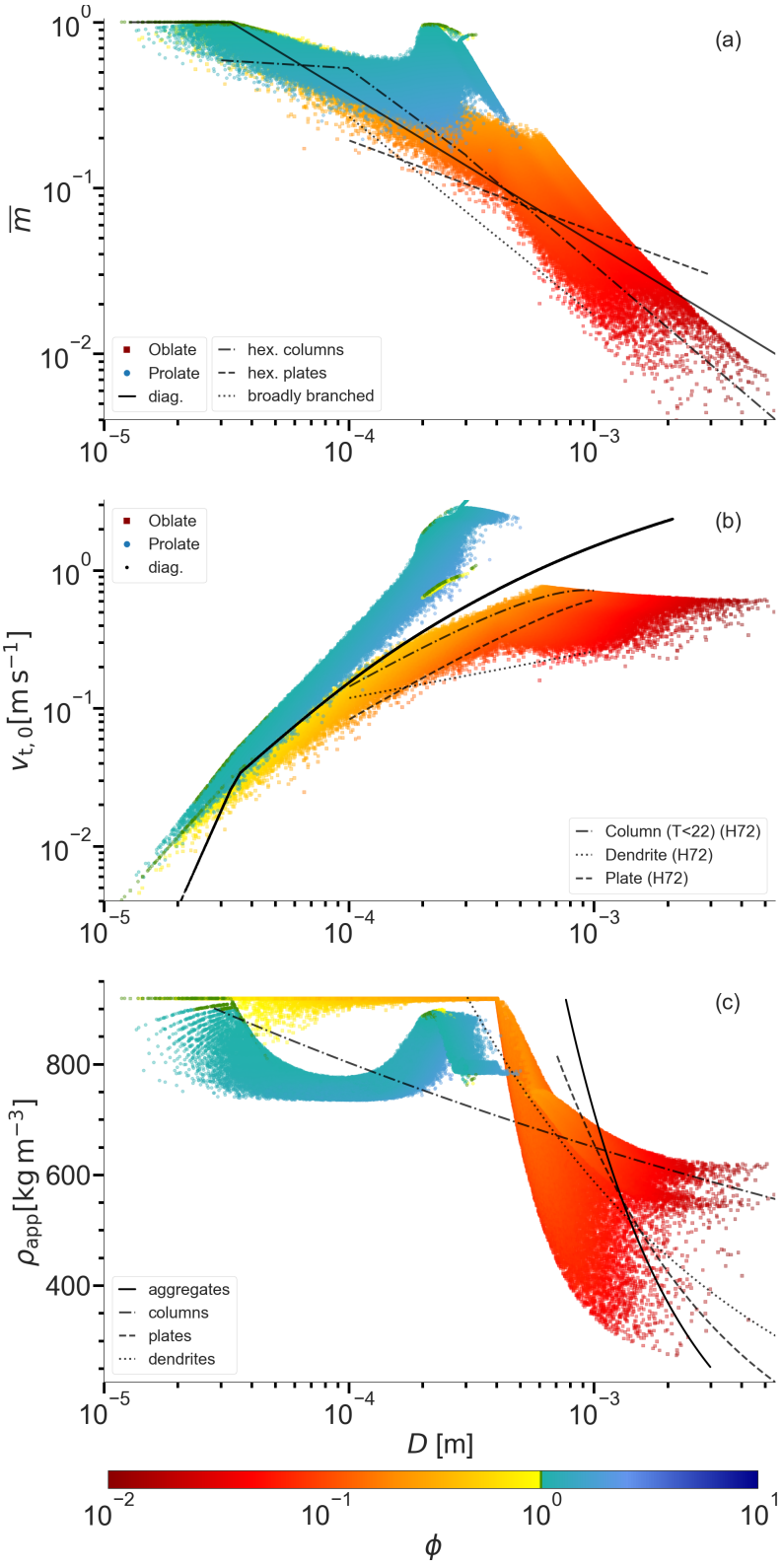

Figure 18. Same as Fig. 16 but using the updated IGF configuration. Lines in (a) are empirical relations of Mitchell (1996), in (b) of A. Heymsfield (1972), and in (c) from Pruppacher and Klett (1997).

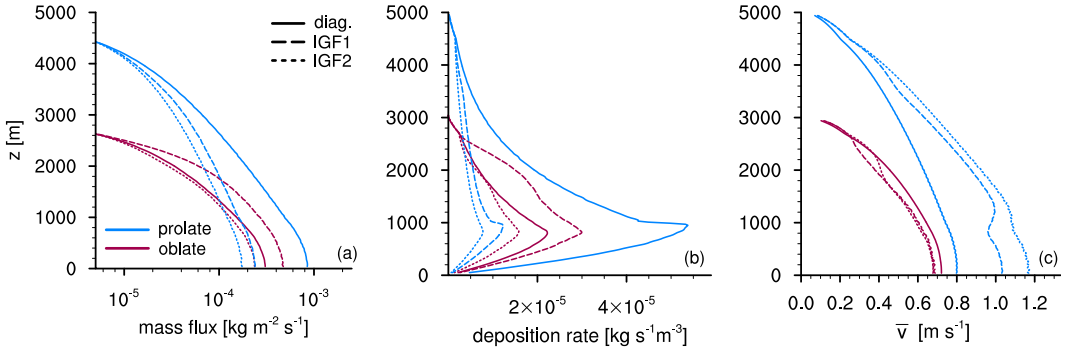

Figure 19. Comparison of vertical profiles of (a) mass flux, (b) deposition rate, and (c) mass-weighted velocity $\overline{v}$ for particles nucleated in a prolate regime (blue, $\Delta z_{\mathrm{nuc}} = 4500 - 5000\,\mathrm{m}$) and an oblate regime (red, $\Delta z_{\mathrm{nuc}} = 2700 - 3000\,\mathrm{m}$) using a diagnostic geometry (solid), HP with original IGF (dashed), and HP with updated IGF (short-dashed).

geometry shortens the residence time. This can only be seen by comparing Fig. 16 and 18 because the mass-weighted velocity (Fig 19c) does not show the effect of the lighter particles. The effect of the two IGF versions on habit development is visualized in Figure 20. For reference, lines are plotted for ϕ-D-relations from Auer and Veal (1970), assuming the corresponding nucleation temperature (columnar (dash-dotted) $T < 253\,\mathrm{K}$, P1e (dashed): $256\,\mathrm{K} < T < 260\,\mathrm{K}$). The ARs of the prolates developed for the original IGF (blue) are similar to those expected from the empirical relations in the corresponding temperature range. Using the new IGF instead, columnar particles develop similar ARs for lower D due to the removal of the size constraint on habit development, but for larger D their ARs are less pronounced and some particles even change their habit (highlighted in light blue). The classification of these particles is difficult, but they could be interpreted as complex polycrystals like capped columns. If they are polycrystals, this raises the question of the apparent density treatment. It seems unlikely that Eq. 7 can describe the development of secondary habits for polycrystalline structures, since for sphericity the deposition densities are at or around ice density.

By removing the size constraint on habit development, planar particles (red) are able to develop strong aspect ratios close to $\phi = 10^{-2}$ (lower right corner) for the updated IGF including modifications. For very large D, the aspect ratios are similar to those expected from the empirical relation for dendrites.

We can conclude that the changes to the IGF and the branching criterion reduce the mass flux for both scenarios while allowing the development of very thin plates. It remains an open question how to deal with particles that change their habit, since the spheroidal approach is limited to simple geometries.

5.3 Aggregation

The three main factors influencing the aggregation process are the geometric area A, the fall velocity difference $\Delta v = |v_1 - v_2|$, and the collision efficiency E_{c}, which depends on the difference in v_{t}. The habit prediction scheme affects all of the above factors by introducing variability in particle shape and density, broadening the velocity spectrum, and potentially changing the cross sectional area. Here, we use the formulation from Mitchell (1988) for sticking efficiency, which prescribes piecewise linear values for temperature ranges. Intuitively, the habit prediction is expected to lead to altered, habit-specific aggregation rates that feedback on depositional growth. Figure 21 shows the vertical profiles of number density (left column) and mass flux (right column) for the oblate (top row) and prolate (bottom row) cases, separated into monomers and aggregates. The

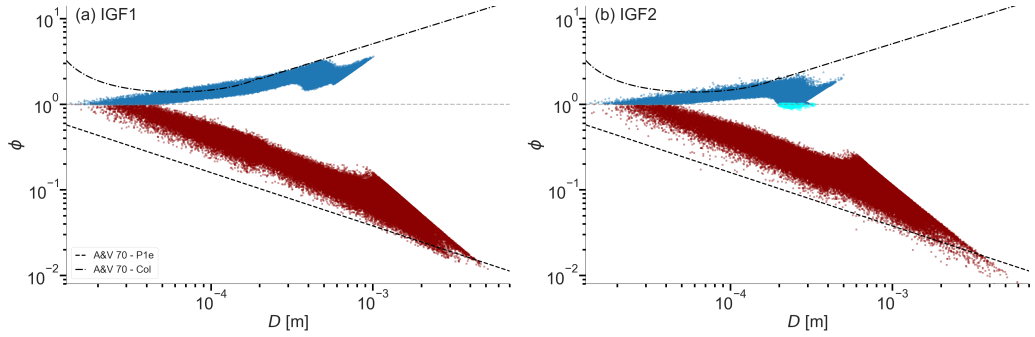

Figure 20. ϕ-D-relations of the two cases for the original IGF (a) and the updated version with modifications (b). The black lines are empirical relations from Auer and Veal (1970).

vertical number density profiles show that the different descriptions of depositional growth and geometry have critical effects on aggregation. The development of dendritic crystals causes an earlier and stronger initial aggregation rate compared to particles without HP and is strongest for the original IGF (crystals branch earlier). Both IGF configurations show a reduction in monomer number density, but the earlier branching critically influences the onset of aggregation and the additional collection of both monomers and aggregates further down. This causes the mass flux for the original IGF to be dominated by aggregates. The number of aggregates for the modified IGF is almost independent of height, indicating that aggregates mainly collect other monomers rather than self-collection of monomers or aggregates. Analysis of the number of monomers per aggregate confirms that mostly large monomers are collected, while smaller crystals rarely aggregate (not shown). Oblate particles grow efficiently by vapor growth and their collection by aggregation does not transfer its positive effects to the aggregates because we assume that their geometry is reduced to the m-D power law. This leads to a reduction in the total mass flux when the HP is compared to the classical m-D-relationship, indicating the effect of the simplified aggregation geometry that immediately forgets the monomer information. A difference between the two IGF configurations for the composition of the total mass flux at the surface is present: for the original IGF, the mass flux is dominated by aggregates and close to equality for the new configuration. The higher total number density leads to more depositional growth because the supersaturation is fixed. If there would be an interactive feedback between hydrometeors and the atmosphere, higher number densities would lead to a faster depletion of the supersaturation.

The prolate case shows the opposite behavior: the reduced depositional growth compared to particles without explicit habit, caused by shorter residence times, leads to smaller cross sectional areas, which in turn decreases the aggregation rates. Particles with a diagnostic geometry, on the other hand, start to aggregate efficiently in the lower half of the domain, where the sticking efficiency is high, so that the number densities of monomers and aggregates constantly decrease and large aggregates form. Aggregates dominate the mass flux when no habits can develop, while for the HP the mass flux is defined by that of the monomers.

The habit prediction has a significant impact on the aggregation of the cases studied. The impact depends on the dominant primary habit, but could be overestimated because in the specific cases no different primary habits coexist that would lead to potentially high aggregation rates.

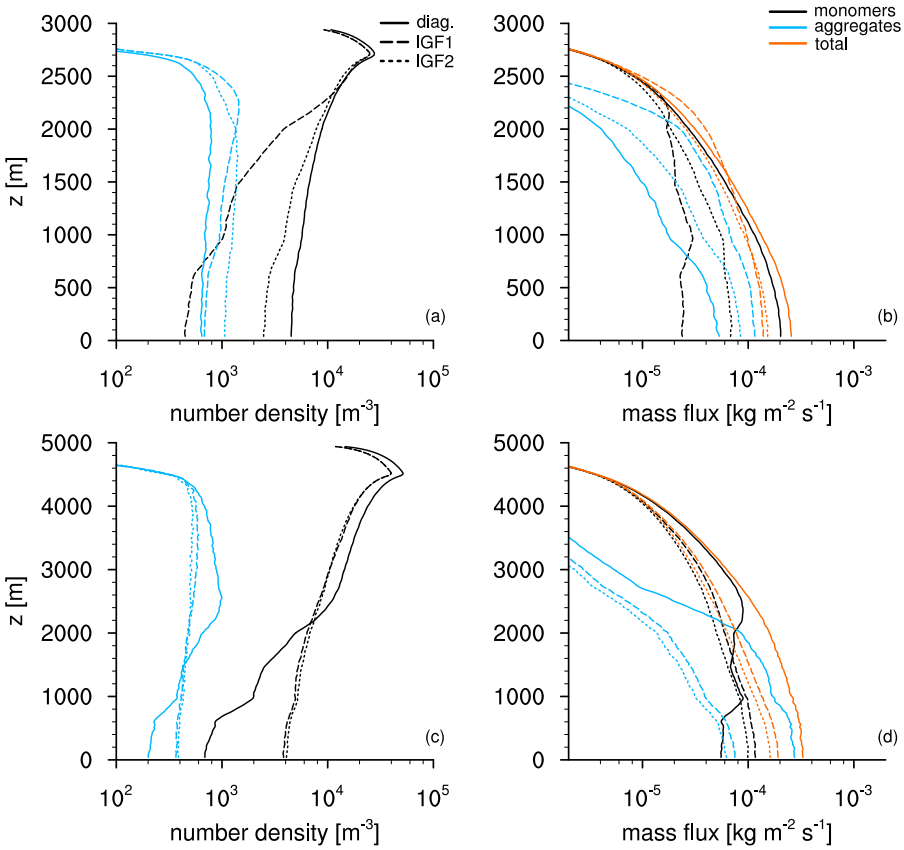

Figure 21. Vertical profiles of number density (a & c) and mass flux (b & d) for monomers (black) and aggregates (blue) for the oblate (top row) and prolate (bottom row) nucleation regimes using a diagnostic geometry (solid), HP with original IGF (dashed), and HP with updated IGF (short-dashed) with deposition and aggregation enabled.

5.4 Riming

Finally, we enable riming by specifying a liquid water zone in the bottom 20% of the domain (Fig. 22). Particles are classified as rimed as soon as they contain rime mass. For low LWCs, the transition from prolate/oblate monomers may be slow, and habit effects caused by deposition may persist, but high LWCs lead to effective rounding of particles, which can then be described by m-D-relations for rimed particles or graupel (as shown by Jensen and Harrington (2015)).

For the chosen conditions, all particles are large enough to rime immediately upon reaching the LWZ, regardless of configuration. Riming increases the mass and area of the particles while accelerating them, increasing the rate of aggregation and leading to a further decrease in number density. The immediate effect of the added rime mass is to fill the porous structures before effectively increasing the maximum dimension. For particles that do not develop a habit, this leads to a dominance of the acceleration effect over the geometric change. Regardless of the primary habit, particles that are allowed to evolve habits are effectively dragged toward sphericity by the assumption that riming only increases the minor dimension (see Eq. 18 & 19). Therefore, riming accelerates the most pronounced evolved habit through mass growth and rounding. IGF configuration has a weak effect on riming compared to deposition and aggregation. Only for prolates following the original IGF can a more pronounced decrease in number density

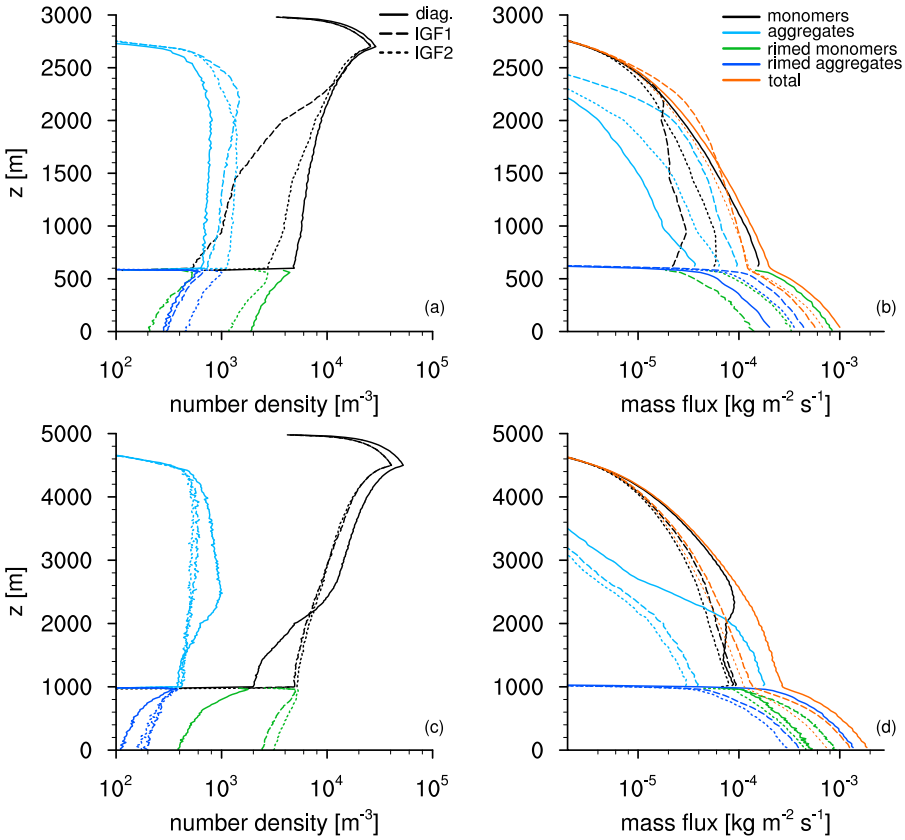

Figure 22. Vertical profiles of number density (a & c) and mass flux (b & d) for monomers (black), aggregates (black), rimed monomers (green), and rimed aggregates (dark blue) for the oblate (top row) and prolate nucleation regimes (bottom row) using a diagnostic geometry (solid), HP with original IGF (dashed), and HP with updated IGF (short-dashed) with all processes enabled.

in the LWZ be observed, because the cross-sectional area is more effectively changed by rounding when more pronounced ARs have developed.

6 Conclusion

The LPM *McSnow* has been expanded by an extended version of the habit prediction scheme of Jensen and Harrington (2015), based on the work of J.-P. Chen and Lamb (1994b). The comprehensive hydrodynamic description of porous spheroids by Böhm adds parameterizations regarding terminal velocity and collision efficiency. We propose a mass-dependent interpolation of the terminal velocity between prolate and cylindrical particles based on the laboratory results of McCorquodale and Westbrook (2021), which overcomes the massive deceleration resulting from the cylindrical assumption of Böhm when transitioning from spherical to prolate or vice versa. A shape-dependent ventilation coefficient has been introduced that combines the results of a collection of recent studies on ventilation of different geometries. While the effect on depositional growth is found to be in the range of a few percent for small particles, for larger particles the ventilation coefficients can increase by a factor of two compared to spheres. The habit prediction scheme in its original version was shown to be in good agreement with individual particle measurements from Takahashi et al. (1991), but also has deficiencies, including the polycrystalline regime, the warm prolate maximum, and the branching criterion used for

oblate particles. A comparison with an independent method using the polarizability ratio of Myagkov, Seifert, Bauer-Pfundstein, and Wandinger (2016) confirmed these findings. Hence, we propose a modified version of the IGF combined with a modified branching criterion. These modifications were found to improve the results under constant conditions in an appropriate way. The importance of explicit habit prediction for deposition, aggregation and, in part, riming was demonstrated in a simplified 1-D snow shaft simulation. Columnar particles fall faster than their counterparts without explicit habits, and the shortened residence time leads to less ice mass, independent of the IGF configuration. The reduced mass translates into rather weak aspect ratios and the resulting smaller cross-sectional areas significantly reduce the aggregation rate. However, riming is highly effective and partially enhances aggregation due to the assumed effective rounding increasing the cross-sectional area. For the original IGF configuration, this effect is most pronounced because of the more pronounced ARs that develop due to the prolate maximum around the nucleation temperature.

The deposition rate of the plates is significantly increased compared to the *m-D*-particles for the original IGF at lower fall velocities, especially for large particles, resulting in a higher mass flux. The planar geometry has a positive effect on the aggregation rate, with the opposite effect observed for prolates. The habit effect is partially mitigated when using the modified branching criterion: particles branch later, stay denser, accelerate more, and grow slower than for the original IGF. In turn, the aggregation rates decrease, but are still higher than when no habits are formed. It remains an open question when oblate particles branch, but the proposed approach showed reasonable results. Future laboratory studies could be aimed at understanding the deposition behavior under unfavorable habit conditions e.g. oblate particles growing in an environment that favors prolate growth.

Finally, large LWCs rapidly transform planar crystals into rimed particles once they reach the onset of riming. If the threshold is already exceeded when entering the LWZ, we do not find a significant effect of habit prediction on riming rates.

Given the importance of ice-microphysical processes in mixed-phase clouds, ice habits are highly influential and affect cloud lifetime. The variability of atmospheric conditions shapes individual particles whose characteristics cannot be generalized by broad classifications. The chosen 1-D scenarios can only describe parts of the impact of an explicit habit prediction on process rates, but they already emphasize that it is of first order. By design, the setup does not allow the atmosphere to change dynamically, but these effects should play a role in the competition for water vapor and ultimately alter precipitation rates. More sophisticated atmospheric simulations could be set up to try to reproduce the interactions between different habits that are present simultaneously. Coupling *McSnow* with the ICON model (Zängl et al., 2015) is a next step in achieving such realistic atmospheric simulations.

In addition, the detailed information on particle properties shall be compared with polarimetric measurements to show the validity of the model and to be used as a numerical laboratory to study microphysical processes in clouds.

Appendix A Boehm's theory

In the following, the reader can find the sets of equations of Böhm's theory to calculate the terminal velocity and collision efficiency using BLT.

A1 Terminal fall velocity

For both oblate and prolate particles, Böhm defines the characteristic length scale as the equatorial diameter $d_{\mathrm{char}} = 2\,a$ instead of the maximum dimension (also men-

tioned by (Shima et al., 2020)).

$$X(m,\phi,q) = \frac{8\,m_\mathrm{i}\,g\,\rho_\mathrm{a}}{\pi\,\mu^2\,\max(\phi;1)\,\max(q^{1/4};q)}, \tag{A1a}$$

$$k(\phi) = \min\left(\max(0.82+0.18\,\phi\,;0.85)\,;\left(0.37+\frac{0.63}{\phi}\right)\,;\frac{1.33}{\max(\log\phi\,;0)+1.19}\right), \tag{A1b}$$

$$\Gamma_\phi = \max\left(1\,;\min(1.98\,;3.76-8.41\phi+9.18\phi^2-3.53\phi^3)\right), \tag{A1c}$$

$$C_\mathrm{DP,S} = \max\left(0.292\,k\,\Gamma_\phi\,;0.492-\frac{0.2}{\sqrt{\phi}}\right), \tag{A1d}$$

$$C_\mathrm{DP} = \max\left(1;q(1.46q-0.46)\right)\,C_\mathrm{DP,S}, \tag{A1e}$$

$$C'_\mathrm{DP} = C_\mathrm{DP}\,\frac{1+(X/X_0)^2}{1+1.6(X/X_0)^2}, \qquad \mathrm{with} X_0 = \begin{cases} 2.8\times10^6, & \text{iceparticles,} \\ 6.7\times10^6, & \text{waterparticles,} \end{cases} \tag{A1f}$$

$$C_\mathrm{D0} = 4.5\,k^2\,\max(\phi\,;1), \tag{A1g}$$

$$\beta = \left[1+\frac{C_\mathrm{DP}}{6\,k}\left(\frac{X'}{C'_\mathrm{DP}}\right)^{1/2}\right]^{1/2}-1, \tag{A1h}$$

$$\gamma = \frac{C_\mathrm{D0}-C_\mathrm{DP}}{4\,C_\mathrm{DP}}, \tag{A1i}$$

$$N_\mathrm{Re} = \frac{6\,k}{C'_\mathrm{DP}}\,\beta^2\left[1+\frac{2\,\beta\,e^{-\beta\,\gamma}}{(2+\beta)(1+\beta)}\right], \tag{A1j}$$

$$C_\mathrm{DI} = \frac{X}{N_\mathrm{Re}^2}-\frac{24\,k}{N_\mathrm{Re}}, \tag{A1k}$$

$$v_\mathrm{t} = \frac{\mu\,N_\mathrm{Re}}{\rho_\mathrm{a}\,d_\mathrm{char}}. \tag{A1l}$$

The used variables are the Best number X, the turbulence modified Best number X', the dynamic viscosity μ, the air density ρ_a, the viscous shape parameter k, a function regarding the aspect ratio Γ_ϕ, the drag coefficient $C_\mathrm{DP,S}$, the drag coefficient fitted for prolates C_DP, the Oseen drag coefficient C_DO, the inertial drag coefficient C_DI, the characteristic length scale d_char, and some helper variables β,γ. The minimum and maximum functions are used to constrain transitions from very oblate over quasi-spherical to very prolate particles. For more details on the derivation, the reader is referred to Böhm (1989) and Böhm (1992a). The middle term of formula A1c is found with and without the square root of the aspect ratio in the denominator (see Eq. 13 in (Böhm, 1992a) and Eq. 9 in (Böhm, 1999)). Analysis indicates that for a consistent transition the version from Böhm (1992a) should be correct while differences are marginal.

A2 Collision efficiency

$$F = \sqrt{G^2+\frac{C_\mathrm{I,1}\,v_\mathrm{I1}^2}{C^*_\mathrm{DI}\,|v_1-v_2|^2}}, \tag{A2a}$$

$$G = \frac{6\,\mu_\mathrm{a}}{\rho_\mathrm{a}\,r^*\,|v_1-v_2|\,C^*_\mathrm{DI}}, \tag{A2b}$$

$$H = \frac{2\,m^*}{\rho_\mathrm{a}\,\pi\,r^{*2}\,C^*_\mathrm{DI}\,\delta}, \tag{A2c}$$

$$v_\mathrm{I1} = \frac{2+j}{4}\,v_1. \tag{A2d}$$

$$\tag{A2e}$$

C^*_DI is the inertial drag coefficient with respect to r^* and the initial velocity while $C_\mathrm{I,1}$ refers to the bigger particle properties. While the latter is determined by Eq. A1l, C^*_DI is found by Eq. A1f-g and

$$C^*_\mathrm{DI} = C'_\mathrm{DP}\left(1+\frac{4}{\beta}\left(1-e^{-\gamma\,\beta}\right)\right), \tag{A3}$$

to match the value of C_DI with the value from Oseen theory at low Reynolds numbers.

The two-body system is characterized by the radius r^*, mass m^*, area of intersection A^*, initial velocity v^*, and boundary layer thickness δ_s^*

$$
\begin{aligned}
r^* &= \tfrac{r_1\, r_2}{r_1+r_2} = \sqrt{A^*/\pi}, && \text{(A4a)}\\
m^* &= \tfrac{m_1\, m_2}{m_1+m_2}, && \text{(A4b)}\\
A^* &= \pi\, r^{*2} = \tfrac{A_1\, A_2}{\pi\,(r_{\mathrm{e}1}+r_{\mathrm{e}2})}, && \text{(A4c)}\\
v^* &= \max\left(|v_1 - v_2|; v_\mathrm{min}\right), && \text{(A4d)}\\
\delta_\mathrm{s}^* &= \delta_{\mathrm{s}1}\sqrt{v_1/v^*} + \delta_{\mathrm{s}2}\sqrt{v_2/v^*}. && \text{(A4e)}
\end{aligned}
$$

For v^*, a minimum value is assumed ($v_\mathrm{min} = 10^{-10}\,\mathrm{m\,s^{-1}}$) because for equally fast particles the difference would approach zero, leading to a division by zero in Eq. A2a and A2b.

In the case of an oblate particle, the equivalent circular radius r_e is the equatorial radius r but for prolate particles the definition changes to

$$
r_\mathrm{e} = \left(\frac{4\,\phi}{\pi}\right)^{1/2} r_1, \tag{A5}
$$

following the special assumptions of columns to be better approximated by a cylindrical shape. In Böhm (1999), he also especially mentions that in case of columns or irregularly shaped aggregates the equivalent circular definition shall be used. In a generalized form for all particle shapes they can be written as

$$
\begin{aligned}
r_\mathrm{e} &= \sqrt{A/\pi}, && \text{(A6a)}\\
\phi_\mathrm{e} &= \min(\phi; 1)\,\tfrac{r}{r_\mathrm{e}}, && \text{(A6b)}\\
q_\mathrm{e} &= \begin{cases} \pi\, q/4, & q > 1,\\ q, & q \le 1, \end{cases} = q\left[1 - \tfrac{\max(q-1;0)}{q-1}\left(1-\tfrac{\pi}{4}\right)\right]. && \text{(A6c)}
\end{aligned}
$$

To fully define the shape characteristics of the two-body system, we additionally need to give definitions of the equivalent aspect ratio and porosity. Simple averaging of these quantities might lead to strong over- or underestimation. Hence, we use the radius weighted mean of those characteristics (Böhm, 1999)

$$
\xi^* = r^*\left(\frac{\xi_1}{r_{e1}} + \frac{\xi_2}{r_{e2}}\right) \qquad (\xi = q, \phi), \tag{A7}
$$

where the indices refer to the corresponding particle.

For anisotropic particles, the velocity v_1 has to be replaced by a characteristic velocity

$$
v_1' = \begin{cases} \phi_1\, v_1 & \text{, forplates,}\\ \frac{3}{4}\, v_1 & \text{, forcolumns.} \end{cases} \tag{A8}
$$

Variables used in the flow correction for potential flow are defined as

$$
\begin{aligned}
t_\delta &= \begin{cases} \frac{c_y}{\Delta_y}\,\arctan\frac{\Delta_y}{b\,c_y - 1}, & (b\,c_y \ge 1),\\ \frac{c_y}{\Delta_y}\,(\pi - \arctan\frac{\Delta_y}{1 - b\,c_y}), & (\frac{1}{2} < b\,c_y < 1), \end{cases} && \text{(A9a)}\\
c_i &= \frac{m_2}{3\,k_{2,i}\,\pi\,r_2\,\eta_\mathrm{a}} \qquad (i = x, y), && \text{(A9b)}\\
b &= \tfrac{3\,v}{r_{\mathrm{e},1}\,\delta_1}, && \text{(A9c)}\\
\Delta_x &= \sqrt{2\,b\,c_x/j + 1}, && \text{(A9d)}\\
\Delta_y &= \sqrt{2\,b\,c_y - 1}. && \text{(A9e)}
\end{aligned}
$$

The shape factor $k_{2,x}$ does not describe the same quantity as in Eq. A1c because this is defined perpendicular to the axis of symmetry in case of a plate or as the arithmetic mean

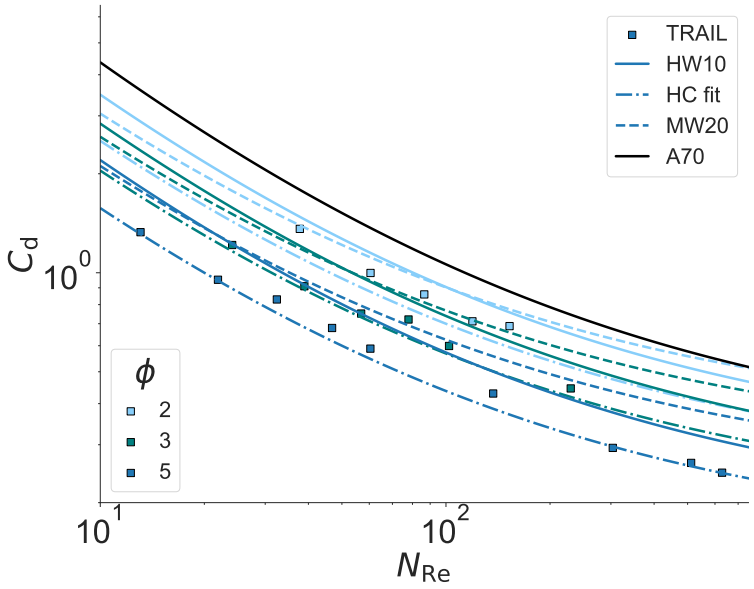

Figure A1. Fits for the N_{Re}-C_{d}-relations compared with data of hexagonal columns from TRAIL (colored squares). Black line corresponds to the solution of spheres by Abraham (1970, A70), solid lines are the generalized relation of A. J. Heymsfield and Westbrook (2010, HW10), dashed lines mark results of McCorquodale and Westbrook (2021, MW20), and dash-dotted lines show our fit for hexagonal columns (HC) only. The assumed aspect ratio is color coded

of the two shape factors parallel and perpendicular to the axis for a column. It can be approximated by

$$k_{2,x} \approx \begin{cases} 0.57 + 0.43\,\phi, & (\phi < 1), \\ k^{1.15}, & (\phi > 1). \end{cases} \tag{A10}$$

A3 Shape assumption for columns

Figure A1 shows fits of Eq. 30 of Abraham (1970, A70), A. J. Heymsfield and Westbrook (2010, HW10), McCorquodale and Westbrook (2021, MW20), and our fit (HC fit) compared against the TRAIL data for hexagonal columns.

Appendix B Open Research

McSnow is part of the ICON modeling framework and the code is available under two different licenses: A personal non-commercial scientific license, and an institutional license that requires a cooperation agreement with DWD. More details on the licenses and an instruction how to obtain the ICON code can be found at `https://code.mpimet.mpg.de/projects/iconpublic`. Access to the McSnow repository can be granted on request as soon as an ICON license agreement has been signed. Data and post-processing script are available from Zenodo at `https://doi.org/10.5281/zenodo.7900348`. The repository includes a modified copy of the data from McCorquodale and Westbrook (2021) found in the "Supporting Information" section]TRAIL2021b.

Acknowledgments

The in-depth analysis of the Böhm parameterization would not have been so fruitful without the data set of the TRAIL campaign. We, therefore, like to thank Christopher D. Westbrook for sharing the data and providing insight. Furthermore, we would like to thank Alexander Myagkov for sharing the routines used to calculate the polarizability ratio from shape and density. This work has been funded by the German Science Foundation (DFG) under grant SE 1784/3-1, project ID 408011764 as part of the DFG priority program SPP 2115 on radar polarimetry.

References

Abraham, F. F. (1970). Functional dependence of drag coefficient of a sphere on reynolds number. *The Physics of Fluids*, *13*(8), 2194-2195. Retrieved from https://aip.scitation.org/doi/abs/10.1063/1.1693218 doi: 10.1063/1.1693218

Auer, A. H., & Veal, D. L. (1970). The dimension of ice crystals in natural clouds. *J. Atmos. Sci*, *27*(6), 919 - 926. Retrieved from https://journals.ametsoc.org/view/journals/atsc/27/6/1520-0469_1970_027_0919_tdoici_2_0_co_2.xml doi: 10.1175/1520-0469(1970)027⟨0919:TDOICI⟩2.0.CO;2

Bailey, M. P., & Hallett, J. (2009, 9). A comprehensive habit diagram for atmospheric ice crystals: Confirmation from the laboratory, airs ii, and other field studies. *J. Atmos. Sci.*, *66*, 2888-2899. Retrieved from http://journals.ametsoc.org/doi/abs/10.1175/2009JAS2883.1 doi: 10.1175/2009JAS2883.1

Baran, A. J. (2012). From the single-scattering properties of ice crystals to climate prediction: A way forward. *Atmos. Res.*, *112*, 45 - 69. Retrieved from http://www.sciencedirect.com/science/article/pii/S0169809512001160 doi: 10.1016/j.atmosres.2012.04.010

Beard, K. V. (1980). The effects of altitude and electrical force on the terminal velocity of hydrometeors. *J. Atmos. Sci*, *37*(6), 1363 - 1374. Retrieved from https://journals.ametsoc.org/view/journals/atsc/37/6/1520-0469_1980_037_1363_teoaae_2_0_co_2.xml doi: 10.1175/1520-0469(1980)037⟨1363:TEOAAE⟩2.0.CO;2

Brdar, S., & Seifert, A. (2018). Mcsnow: A monte-carlo particle model for riming and aggregation of ice particles in a multidimensional microphysical phase space. *J. Adv. Model Earth Sy.*, *10*(1), 187-206. Retrieved from https://agupubs.onlinelibrary.wiley.com/doi/abs/10.1002/2017MS001167 doi: 10.1002/2017MS001167

Bringi, V., Seifert, A., Wu, W., Thurai, M., Huang, G. J., & Siewert, C. (2020, 8). Hurricane dorian outer rain band observations and 1d particle model simulations: A case study. *Atmosphere*, *11*, 879. Retrieved from https://www.mdpi.com/2073-4433/11/8/879/htm doi: 10.3390/ATMOS11080879

Böhm, J. P. (1989). A general equation for the terminal fall speed of solid hydrometeors. *J. Atmos. Sci.*, *46*(15), 2419-2427. Retrieved from https://doi.org/10.1175/1520-0469(1989)046<2419:AGEFTT>2.0.CO;2 doi: 10.1175/1520-0469(1989)046⟨2419:AGEFTT⟩2.0.CO;2

Böhm, J. P. (1990). *On the hydrodynamics of cloud and precipitation particles* (Doctoral dissertation, ETH Zurich). doi: 10.3929/ethz-a-000578177

Böhm, J. P. (1992a). A general hydrodynamic theory for mixed-phase microphysics. part i: drag and fall speed of hydrometeors. *Atmos. Res.*, *27*(4), 253 - 274. Retrieved from http://www.sciencedirect.com/science/article/pii/0169809592900359 doi: 10.1016/0169-8095(92)90035-9

Böhm, J. P. (1992b). A general hydrodynamic theory for mixed-phase microphysics. part ii: collision kernels for coalescence. *Atmos. Res.*, *27*(4), 275 - 290. Retrieved from http://www.sciencedirect.com/science/article/pii/

0169809592900036A doi: 10.1016/0169-8095(92)90036-A

Böhm, J. P. (1992c). A general hydrodynamic theory for mixed-phase microphysics. part iii: Riming and aggregation. *Atmos. Res.*, *28*(2), 103 - 123. Retrieved from http://www.sciencedirect.com/science/article/pii/0169809592900234 doi: 10.1016/0169-8095(92)90023-4

Böhm, J. P. (1994). Theoretical collision efficiencies for riming and aerosol impaction. *Atmos. Res.*, *32*(1), 171 - 187. Retrieved from http://www.sciencedirect.com/science/article/pii/0169809594900582 doi: 10.1016/0169-8095(94)90058-2

Böhm, J. P. (1999). Revision and clarification of "a general hydrodynamic theory for mixed-phase microphysics". *Atmos. Res.*, *52*(3), 167 - 176. Retrieved from http://www.sciencedirect.com/science/article/pii/S0169809599000332 doi: 10.1016/S0169-8095(99)00033-2

Böhm, J. P. (2004). Reply to comment on "revision and clarification of 'a general hydrodynamic theory for mixed-phase microphysics' [böhm j.p., 1999, atmos. res. 52, 167–176]". *Atmos. Res.*, *69*(3), 289 - 293. Retrieved from http://www.sciencedirect.com/science/article/pii/S016980950300125X doi: 10.1016/j.atmosres.2003.10.001

Chen, J.-P., & Lamb, D. (1994a, 09). Simulation of Cloud Microphysical and Chemical Processes Using a Multicomponent Framework. Part I: Description of the Microphysical Model. *J. Atmos. Sci.*, *51*(18), 2613-2630. Retrieved from https://doi.org/10.1175/1520-0469(1994)051<2613:SOCMAC>2.0.CO;2 doi: 10.1175/1520-0469(1994)051⟨2613:SOCMAC⟩2.0.CO;2

Chen, J.-P., & Lamb, D. (1994b). The theoretical basis for the parameterization of ice crystal habits: Growth by vapor deposition. *J. Atmos. Sci.*, *51*(9), 1206-1222. Retrieved from https://doi.org/10.1175/1520-0469(1994)051<1206:TTBFTP>2.0.CO;2 doi: 10.1175/1520-0469(1994)051⟨1206:TTBFTP⟩2.0.CO;2

Chen, Y., Jiang, P., Xiong, T., Wei, W., Fang, Z., & Wang, B. (2021, 11). Drag and heat transfer coefficients for axisymmetric nonspherical particles: A lbm study. *Chem. Eng. J.*, *424*, 130391. doi: 10.1016/J.CEJ.2021.130391

Connolly, P. J., Emersic, C., & Field, P. R. (2012). A laboratory investigation into the aggregation efficiency of small ice crystals. *Atmos. Chem. Phys.*, *12*, 2055-2076. doi: 10.5194/acp-12-2055-2012

Dias Neto, J., Kneifel, S., Ori, D., Trömel, S., Handwerker, J., Bohn, B., ... Simmer, C. (2019). The triple-frequency and polarimetric radar experiment for improving process observations of winter precipitation. *Earth Syst. Sci Data*, *11*(2), 845–863. Retrieved from https://essd.copernicus.org/articles/11/845/2019/ doi: 10.5194/essd-11-845-2019

Dziekan, P., Waruszewski, M., & Pawlowska, H. (2019, 7). University of warsaw lagrangian cloud model (uwlcm) 1.0: a modern large-eddy simulation tool for warm cloud modeling with lagrangian microphysics. *Geosci. Model Dev.*, *12*, 2587-2606. Retrieved from https://www.geosci-model-dev.net/12/2587/2019/ doi: 10.5194/gmd-12-2587-2019

Field, P. R., Hogan, R. J., Brown, P. R. A., Illingworth, A. J., Choularton, T. W., Kaye, P. H., ... Greenaway, R. (2004). Simultaneous radar and aircraft observations of mixed-phase cloud at the 100 m scale. *Q. J. Roy. Meteor. Soc.*, *130*(600), 1877-1904. Retrieved from https://rmets.onlinelibrary.wiley.com/doi/abs/10.1256/qj.03.102 doi: 10.1256/qj.03.102

Fukuta, N. (1969). Experimental studies on the growth of small ice crystals. *J. Atmos. Sci.*, *26*(3), 522-531. Retrieved from https://doi.org/10.1175/1520-0469(1969)026<0522:ESOTGO>2.0.CO;2 doi: 10.1175/1520-0469(1969)026⟨0522:ESOTGO⟩2.0.CO;2

Gavze, E., & Khain, A. (2022). Gravitational collision of small nonspherical particles: Swept volumes of prolate and oblate spheroids in calm air. *J. Atmos. Sci.*, *79*(6), 1493 - 1514. Retrieved from https://journals

.ametsoc.org/view/journals/atsc/79/6/JAS-D-20-0336.1.xml doi: 10.1175/JAS-D-20-0336.1

Hall, W. D., & Pruppacher, H. R. (1976). The survival of ice particles falling from cirrus clouds in subsaturated air. *J. Atmos. Sci.*, *33*(10), 1995-2006. Retrieved from https://doi.org/10.1175/1520-0469(1976)033<1995:TSOIPF>2.0.CO;2 doi: 10.1175/1520-0469(1976)033⟨1995:TSOIPF⟩2.0.CO;2

Harrington, J. Y., Moyle, A., Hanson, L. E., & Morrison, H. (2019). On calculating deposition coefficients and aspect-ratio evolution in approximate models of ice crystal vapor growth. *J. Atmos. Sci.*, *76*(6), 1609-1625. Retrieved from https://doi.org/10.1175/JAS-D-18-0319.1 doi: 10.1175/JAS-D-18-0319.1

Hashino, T., & Tripoli, G. J. (2007). The spectral ice habit prediction system (ships). part i: Model description and simulation of the vapor deposition process. *J. Atmos. Sci.*, *64*(7), 2210 - 2237. Retrieved from https://journals.ametsoc.org/view/journals/atsc/64/7/jas3963.1.xml doi: 10.1175/JAS3963.1

Heymsfield, A. (1972). Ice crystal terminal velocities. *J. Atmos. Sci*, *29*, 1348-1357. Retrieved from https://journals.ametsoc.org/view/journals/atsc/29/7/1520-0469_1972_029_1348_ictv_2_0_co_2.xml doi: 10.1175/1520-0469(1972)029⟨1348:ICTV⟩2.0.CO;2

Heymsfield, A. J. (1978). The characteristics of graupel particles in northeastern colorado cumulus congestus clouds. *J. Atmos. Sci.*, *35*(2), 284-295. Retrieved from https://journals.ametsoc.org/doi/abs/10.1175/1520-0469%281978%29035%3C0284%3ATCOGPI%3E2.0.CO%3B2 doi: 10.1175/1520-0469(1978)035⟨0284:TCOGPI⟩2.0.CO;2

Heymsfield, A. J., & Westbrook, C. D. (2010, 08). Advances in the Estimation of Ice Particle Fall Speeds Using Laboratory and Field Measurements. *J. Atmos. Sci.*, *67*(8), 2469-2482. Retrieved from https://doi.org/10.1175/2010JAS3379.1 doi: 10.1175/2010JAS3379.1

Jayaweera, K. O. L. F., & Cottis, R. E. (1969). Fall velocities of plate-like and columnar ice crystals. *Q. J. Roy. Meteor. Soc.*, *95*(406), 703-709. Retrieved from https://rmets.onlinelibrary.wiley.com/doi/abs/10.1002/qj.49709540604 doi: 10.1002/qj.49709540604

Jensen, A. A., & Harrington, J. Y. (2015). Modeling ice crystal aspect ratio evolution during riming: A single-particle growth model. *J. Atmos. Sci.*, *72*(7), 2569-2590. Retrieved from https://doi.org/10.1175/JAS-D-14-0297.1 doi: 10.1175/JAS-D-14-0297.1

Jensen, A. A., Harrington, J. Y., Morrison, H., & Milbrandt, J. A. (2017, 6). Predicting ice shape evolution in a bulk microphysics model. *J. Atmos. Sci.*, *74*, 2081-2104. Retrieved from https://journals.ametsoc.org/view/journals/atsc/74/6/jas-d-16-0350.1.xml doi: 10.1175/JAS-D-16-0350.1

Ji, W., & Wang, P. K. (1999). Ventilation coefficients for falling ice crystals in the atmosphere at low-intermediate reynolds numbers. *J. Atmos. Sci.*, *56*, 829-836. doi: 10.1175/1520-0469(1999)056⟨0829:VCFFIC⟩2.0.CO;2

Karrer, M., Seifert, A., Ori, D., & Kneifel, S. (2021). Improving the representation of aggregation in a two-moment microphysical scheme with statistics of multi-frequency doppler radar observations. *Atmos. Chem. Phys.*, *21*(22), 17133–17166. Retrieved from https://acp.copernicus.org/articles/21/17133/2021/ doi: 10.5194/acp-21-17133-2021

Ke, C., Shu, S., Zhang, H., Yuan, H., & Yang, D. (2018, 2). On the drag coefficient and averaged nusselt number of an ellipsoidal particle in a fluid. *Powder Technol.*, *325*, 134-144. doi: 10.1016/J.POWTEC.2017.10.049

Kikuchi, K., Kameda, T., Higuchi, K., & Yamashita, A. (2013). A global classification of snow crystals, ice crystals, and solid precipitation based on observations from middle latitudes to polar regions. *Atmos. Res.*, *132-133*, 460-472. Re-

trieved from https://www.sciencedirect.com/science/article/pii/S0169809513001841 doi: 10.1016/j.atmosres.2013.06.006

Kintea, D. M., Roisman, I. V., Hauk, T., & Tropea, C. (2015, 9). Shape evolution of a melting nonspherical particle. *Physical Review E - Statistical, Nonlinear, and Soft Matter Physics*, *92*. doi: 10.1103/PhysRevE.92.033012

Kiwitt, T., Fröhlich, K., Meinke, M., & Schröder, W. (2022, 4). Nusselt correlation for ellipsoidal particles. *Int. J. Multiphas. Flow*, *149*, 103941. doi: 10.1016/J.IJMULTIPHASEFLOW.2021.103941

Kobayashi, T. (1961). The growth of snow crystals at low supersaturations. *Philos. Mag.*, *6*(71), 1363-1370. Retrieved from https://doi.org/10.1080/14786436108241231 doi: 10.1080/14786436108241231

Korolev, A., & Isaac, G. (2003). Roundness and aspect ratio of particles in ice clouds. *J. Atmos. Sci.*, *60*(15), 1795-1808. Retrieved from https://doi.org/10.1175/1520-0469(2003)060<1795:RAAROP>2.0.CO;2 doi: 10.1175/1520-0469(2003)060⟨1795:RAAROP⟩2.0.CO;2

Lawson, R. P., Pilson, B., Baker, B., Mo, Q., Jensen, E., Pfister, L., & Bui, P. (2008). Aircraft measurements of microphysical properties of subvisible cirrus in the tropical tropopause layer. *Atmos. Chem. Phys.*, *8*(6), 1609–1620. Retrieved from https://www.atmos-chem-phys.net/8/1609/2008/ doi: 10.5194/acp-8-1609-2008

Locatelli, J. D., & Hobbs, P. V. (1974). Fall speeds and masses of solid precipitation particles. *J. Geophys. Res.*, *79*(15), 2185-2197. Retrieved from https://agupubs.onlinelibrary.wiley.com/doi/abs/10.1029/JC079i015p02185 doi: 10.1029/JC079i015p02185

Martin, J. J., Wang, P. K., Pruppacher, H. R., & Pitter, R. L. (1981). Numerical study of the effect of electric charges on the efficenciy with which planar ice crystals collect supercooled cloud drops. *J. Atmos. Sci.*, *38*(11), 2462-2469. doi: 10.1175/1520-0469(1981)038⟨2462:ANSOTE⟩2.0.CO;2

Matrosov, S. Y., Mace, G. G., Marchand, R., Shupe, M. D., Hallar, A. G., & Mccubbin, I. B. (2012, 8). Observations of ice crystal habits with a scanning polarimetric w-band radar at slant linear depolarization ratio mode. *J. Atmos. Ocean Tech.*, *29*, 989-1008. Retrieved from https://journals.ametsoc.org/view/journals/atot/29/8/jtech-d-11-00131_1.xml doi: 10.1175/JTECH-D-11-00131.1

McCorquodale, M. W., & Westbrook, C. D. (2021). Trail part 2: A comprehensive assessment of ice particle fall speed parametrisations. *Q. J. Roy. Meteor. Soc.*, *147*(734), 605-626. Retrieved from https://rmets.onlinelibrary.wiley.com/doi/abs/10.1002/qj.3936 doi: 10.1002/qj.3936

Melnikov, V., & Straka, J. M. (2013, 8). Axis ratios and flutter angles of cloud ice particles: Retrievals from radar data. *J. Atmos. Ocean Tech.*, *30*, 1691-1703. Retrieved from https://journals.ametsoc.org/view/journals/atot/30/8/jtech-d-12-00212_1.xml doi: 10.1175/JTECH-D-12-00212.1

Milbrandt, J. A., Morrison, H., II, D. T. D., & Paukert, M. (2021). A triple-moment representation of ice in the predicted particle properties (p3) microphysics scheme. *J. Atmos. Sci.*, *78*(2), 439 - 458. Retrieved from https://journals.ametsoc.org/view/journals/atsc/78/2/jas-d-20-0084.1.xml doi: 10.1175/JAS-D-20-0084.1

Mitchell, D. L. (1988). Evolution of snow-size spectra in cyclonic storms. part i: Snow growth by vapor deposition and aggregation. *J. Atmos. Sci.*, *45*, 3431-3451. doi: 10.1175/1520-0469(1988)045⟨3431:EOSSSI⟩2.0.CO;2

Mitchell, D. L. (1996). Use of mass- and area-dimensional power laws for determining precipitation particle terminal velocities. *J. Atmos. Sci.*, *53*(12), 1710-1723. Retrieved from https://doi.org/10.1175/1520-0469(1996)053<1710:UOMAAD>2.0.CO;2 doi: 10.1175/1520-0469(1996)053⟨1710:UOMAAD⟩2.0.CO;2

Mitra, S. K., Vohl, O., Ahr, M., & Pruppacher, H. R. (1990). A wind tunnel and theoretical study of the melting behavior of atmospheric ice particles. iv: Experiment and theory for snow flakes. *J. Atmos. Sci*, *47*(5), 584 - 591. Retrieved from https://journals.ametsoc.org/view/journals/atsc/47/5/1520-0469_1990_047_0584_awtats_2_0_co_2.xml doi: 10.1175/1520-0469(1990)047⟨0584:AWTATS⟩2.0.CO;2

Morrison, H., de Boer, G., Feingold, G., Harrington, J., Shupe, M. D., & Sulia, K. (2012, 12). Resilience of persistent arctic mixed-phase clouds. *Nat. Geosci.*, *5*, 11-17. Retrieved from https://www.nature.com/articles/ngeo1332 doi: 10.1038/ngeo1332

Morrison, H., & Grabowski, W. W. (2008). A novel approach for representing ice microphysics in models: Description and tests using a kinematic framework. *J. Atmos. Sci.*, *65*(5), 1528 - 1548. Retrieved from https://journals.ametsoc.org/view/journals/atsc/65/5/2007jas2491.1.xml doi: 10.1175/2007JAS2491.1

Morrison, H., van Lier-Walqui, M., Fridlind, A. M., Grabowski, W. W., Harrington, J. Y., Hoose, C., ... Xue, L. (2020). Confronting the challenge of modeling cloud and precipitation microphysics. *J. Adv. Model Earth Sy.*, *12*(8), e2019MS001689. Retrieved from https://agupubs.onlinelibrary.wiley.com/doi/abs/10.1029/2019MS001689 doi: 10.1029/2019MS001689

Myagkov, A., Seifert, P., Bauer-Pfundstein, M., & Wandinger, U. (2016, 2). Cloud radar with hybrid mode towards estimation of shape and orientation of ice crystals. *Atmos. Meas. Tech.*, *9*, 469-489. doi: 10.5194/AMT-9-469-2016

Myagkov, A., Seifert, P., Wandinger, U., Bühl, J., & Engelmann, R. (2016, 8). Relationship between temperature and apparent shape of pristine ice crystals derived from polarimetric cloud radar observations during the accept campaign. *Atmos. Meas. Tech.*, *9*, 3739-3754. doi: 10.5194/AMT-9-3739-2016

Naumann, A. K., & Seifert, A. (2015). A lagrangian drop model to study warm rain microphysical processes in shallow cumulus. *J. Adv. Model Earth Sy.*, *7*(3), 1136-1154. Retrieved from https://agupubs.onlinelibrary.wiley.com/doi/abs/10.1002/2015MS000456 doi: 10.1002/2015MS000456

Nelson, J. (1998). Sublimation of ice crystals. *J. Atmos. Sci.*, *55*(5), 910-919. Retrieved from https://doi.org/10.1175/1520-0469(1998)055<0910:SOIC>2.0.CO;2 doi: 10.1175/1520-0469(1998)055⟨0910:SOIC⟩2.0.CO;2

Nelson, J. T., & Baker, M. B. (1996). New theoretical framework for studies of vapor growth and sublimation of small ice crystals in the atmosphere. *J. Geophys. Res.: Atmospheres*, *101*(D3), 7033-7047. Retrieved from https://agupubs.onlinelibrary.wiley.com/doi/abs/10.1029/95JD03162 doi: 10.1029/95JD03162

Nettesheim, J. J., & Wang, P. K. (2018, 9). A numerical study on the aerodynamics of freely falling planar ice crystals. *J. Atmos. Sci.*, *75*, 2849-2865. Retrieved from https://journals.ametsoc.org/view/journals/atsc/75/9/jas-d-18-0041.1.xml doi: 10.1175/JAS-D-18-0041.1

Oseen, C. W. (1927). *Neuere methoden und ergebnisse in der hydrodynamik*. Akad. Verlagsgesellschaft Leipzig. Retrieved from https://archive.org/details/in.ernet.dli.2015.80409

Pinsky, M., Khain, A., & Shapiro, M. (2001). Collision efficiency of drops in a wide range of reynolds numbers: Effects of pressure on spectrum evolution. *J. Atmos. Sci.*, *58*(7), 742 - 764. Retrieved from https://journals.ametsoc.org/view/journals/atsc/58/7/1520-0469_2001_058_0742_ceodia_2.0.co_2.xml doi: 10.1175/1520-0469(2001)058⟨0742:CEODIA⟩2.0.CO;2

Pitter, R. L., Pruppacher, H. R., & Hamielec, A. E. (1974). A numerical study of the effect of forced convection on mass transport from a thin oblate spheroid of ice in air. *J. Atmos. Sci.*, *31*, 1058-1066. doi: 10.1175/1520-0469(1974)031⟨1058:ANSOTE⟩2.0.CO;2

Posselt, R., Simmel, M., & Wurzler, S. (2004). Comment on revision and clarification of "a general hydrodynamic theory for mixed-phase microphysics" [böhm, j.p., 1999, atmos. res. 52, 167–176]. *Atmos. Res.*, *69*(3), 281 - 287. Retrieved from http://www.sciencedirect.com/science/article/pii/S0169809503001248 doi: 10.1016/j.atmosres.2003.03.001

Pruppacher, H., & Klett, J. (1997). *Microphysics of clouds and precipitation.* Springer Netherlands. doi: 10.1007/978-0-306-48100-0

Reinking, R. F. (1979). The onset and early growth of snow crystals by accretion of droplets. *J. Atmos. Sci*, *36*, 870 - 881. Retrieved from https://journals.ametsoc.org/view/journals/atsc/36/5/1520-0469_1979_036_0870_toaego_2_0_co_2.xml doi: 10.1175/1520-0469(1979)036⟨0870:TOAEGO⟩2.0.CO;2

Schlamp, R., Pruppacher, H., & Hamielec, A. (1975). A numerical investigation of the efficiency with which simple columnar ice crystals collide with supercooled water drops. *J. Atmos. Sci.*, *32*(12), 2330-2337. doi: 10.1175/1520-0469(1975)032⟨2330:ANIOTE⟩2.0.CO;2

Sei, T., & Gonda, T. (1989). The growth mechanism and the habit change of ice crystals growing from the vapor phase. *J. Cryst. Growth*, *94*(3), 697-707. Retrieved from https://www.sciencedirect.com/science/article/pii/0022024889900948 doi: 10.1016/0022-0248(89)90094-8

Seifert, A., Leinonen, J., Siewert, C., & Kneifel, S. (2019). The geometry of rimed aggregate snowflakes: A modeling study. *J. Adv. Model Earth Sy.*, *11*(3), 712-731. Retrieved from https://agupubs.onlinelibrary.wiley.com/doi/abs/10.1029/2018MS001519 doi: 10.1029/2018MS001519

Sheridan, L. M. (2008). *Deposition coefficient, habit, and ventilation influences on cirriform cloud properties* (Master's thesis, Dept.of Meteorology, The Pennsylvanian State University). Retrieved from https://etda.libraries.psu.edu/catalog/8556

Sheridan, L. M., Harrington, J. Y., Lamb, D., & Sulia, K. (2009). Influence of ice crystal aspect ratio on the evolution of ice size spectra during vapor depositional growth. *J. Atmos. Sci.*, *66*(12), 3732-3743. Retrieved from https://doi.org/10.1175/2009JAS3113.1 doi: 10.1175/2009JAS3113.1

Shima, S., Kusano, K., Kawano, A., Sugiyama, T., & Kawahara, S. (2009, 7). The super-droplet method for the numerical simulation of clouds and precipitation: a particle-based and probabilistic microphysics model coupled with a non-hydrostatic model. *Q. J. Roy. Meteor. Soc.*, *135*, 1307-1320. Retrieved from http://doi.wiley.com/10.1002/qj.441 doi: 10.1002/qj.441

Shima, S., Sato, Y., Hashimoto, A., & Misumi, R. (2020). Predicting the morphology of ice particles in deep convection using the super-droplet method: development and evaluation of scale-sdm 0.2.5-2.2.0, -2.2.1, and -2.2.2. *Geosci. Model Dev.*, *13*(9), 4107–4157. Retrieved from https://gmd.copernicus.org/articles/13/4107/2020/ doi: 10.5194/gmd-13-4107-2020

Sulia, K. J., & Harrington, J. Y. (2011, 11). Ice aspect ratio influences on mixed-phase clouds: Impacts on phase partitioning in parcel models. *J. Geophys. Res.: Atmospheres*, *116*, 21309. Retrieved from https://onlinelibrary.wiley.com/doi/full/10.1029/2011JD016298https://onlinelibrary.wiley.com/doi/abs/10.1029/2011JD016298https://agupubs.onlinelibrary.wiley.com/doi/10.1029/2011JD016298 doi: 10.1029/2011JD016298

Sutherland, W. (1893). Lii. the viscosity of gases and molecular force. *The London, Edinburgh, and Dublin Philosophical Magazine and Journal of Science*, *36*(223), 507-531. Retrieved from https://doi.org/10.1080/14786449308620508 doi: 10.1080/14786449308620508

Takahashi, T., Endoh, T., Wakahama, G., & Fukuta, N. (1991). Vapor diffusional growth of free-falling snow crystals between -3 and −23°c. *J. Meteorol. Soc. Jpn. Ser. II*, *69*(1), 15-30. doi: 10.2151/jmsj1965.69.1_15

Takahashi, T., & Fukuta, N. (1988). Supercooled cloud tunnel studies on the growth of snow crystals between-4 and-20°c. *J. Meteorol. Soc. Jpn. Ser. II*, *66*, 841-855. Retrieved from https://www.jstage.jst.go.jp/article/jmsj1965/66/6/66_6_841/_article doi: 10.2151/jmsj1965.66.6_841

Tridon, F., Battaglia, A., Chase, R. J., Turk, F. J., Leinonen, J., Kneifel, S., ... Nesbitt, S. W. (2019). The microphysics of stratiform precipitation during olympex: Compatibility between triple-frequency radar and airborne in situ observations. *J. Geophys. Res.: Atmospheres*, *124*(15), 8764-8792. Retrieved from https://agupubs.onlinelibrary.wiley.com/doi/abs/10.1029/2018JD029858 doi: 10.1029/2018JD029858

Trömel, S., Simmer, C., Blahak, U., Blanke, A., Doktorowski, S., Ewald, F., ... Quaas, J. (2021). Overview: Fusion of radar polarimetry and numerical atmospheric modelling towards an improved understanding of cloud and precipitation processes. *Atmos. Chem. Phys.*, *21*(23), 17291–17314. Retrieved from https://acp.copernicus.org/articles/21/17291/2021/ doi: 10.5194/acp-21-17291-2021

Um, J., McFarquhar, G. M., Hong, Y. P., Lee, S.-S., Jung, C. H., Lawson, R. P., & Mo, Q. (2015). Dimensions and aspect ratios of natural ice crystals. *Atmos. Chem. Phys.*, *15*(7), 3933–3956. Retrieved from https://acp.copernicus.org/articles/15/3933/2015/ doi: 10.5194/acp-15-3933-2015

von Terzi, L., Neto, J. D., Ori, D., Myagkov, A., & Kneifel, S. (2022, 9). Ice microphysical processes in the dendritic growth layer: a statistical analysis combining multi-frequency and polarimetric doppler cloud radar observations. *Atmos. Chem. Phys.*, *22*, 11795-11821. doi: 10.5194/ACP-22-11795-2022

Wang, P. K. (2021). *Motions of ice hydrometeors in the atmosphere*. Springer Singapore. Retrieved from https://link.springer.com/10.1007/978-981-33-4431-0 doi: 10.1007/978-981-33-4431-0

Wang, P. K., & Ji, W. (2000, 04). Collision Efficiencies of Ice Crystals at Low–Intermediate Reynolds Numbers Colliding with Supercooled Cloud Droplets: A Numerical Study. *J. Atmos. Sci.*, *57*(8), 1001-1009. Retrieved from https://doi.org/10.1175/1520-0469(2000)057<1001:CEOICA>2.0.CO;2 doi: 10.1175/1520-0469(2000)057⟨1001:CEOICA⟩2.0.CO;2

Westbrook, C. D., Hogan, R. J., Illingworth, A. J., Westbrook, C. D., Hogan, R. J., & Illingworth, A. J. (2008, 1). The capacitance of pristine ice crystals and aggregate snowflakes. *J. Atmos. Sci.*, *65*, 206-219. Retrieved from http://journals.ametsoc.org/doi/abs/10.1175/2007JAS2315.1 doi: 10.1175/2007JAS2315.1

Westbrook, C. D., & Sephton, E. K. (2017). Using 3-d-printed analogues to investigate the fall speeds and orientations of complex ice particles. *Geophys. Res. Lett.s*, *44*(15), 7994-8001. Retrieved from https://agupubs.onlinelibrary.wiley.com/doi/abs/10.1002/2017GL074130 doi: 10.1002/2017GL074130

Whitaker, S. (1972, 3). Forced convection heat transfer correlations for flow in pipes, past flat plates, single cylinders, single spheres, and for flow in packed beds and tube bundles. *AIChE Journal*, *18*, 361-371. Retrieved from https://onlinelibrary.wiley.com/doi/full/10.1002/aic.690180219https://onlinelibrary.wiley.com/doi/abs/10.1002/aic.690180219https://aiche.onlinelibrary.wiley.com/doi/10.1002/aic.690180219 doi: 10.1002/AIC.690180219

Woo, S. E., & Hamielec, A. E. (1971). A numerical method of determining the rate of evaporation of small water drops falling at terminal velocity in air. *J. Atmos. Sci.*, *28*, 1448-1454. doi: 10.1175/1520-0469(1971)028⟨1448:ANMODT⟩2.0.CO;2

Zängl, G., Reinert, D., Rípodas, P., & Baldauf, M. (2015). The icon (icosahedral non-hydrostatic) modelling framework of dwd and mpi-m: Description of the non-hydrostatic dynamical core. *Q. J. Roy. Meteor. Soc.*. doi:

1233 10.1002/qj.2378